Precise measurement of the top-quark mass from lepton + jets events at D0

V. M. Abazov,[35] B. Abbott,[73] B. S. Acharya,[29] M. Adams,[49] T. Adams,[47] G. D. Alexeev,[35] G. Alkhazov,[39] A. Alton,[61] G. Alverson,[60] G. A. Alves,[2] L. S. Ancu,[34] M. Aoki,[48] M. Arov,[58] A. Askew,[47] B. Åsman,[41] O. Atramentov,[65] C. Avila,[8] J. BackusMayes,[80] F. Badaud,[13] L. Bagby,[48] B. Baldin,[48] D. V. Bandurin,[47] S. Banerjee,[29] E. Barberis,[60] P. Baringer,[56] J. Barreto,[3] J. F. Bartlett,[48] U. Bassler,[18] V. Bazterra,[49] S. Beale,[6] A. Bean,[56] M. Begalli,[3] M. Begel,[71] C. Belanger-Champagne,[41] L. Bellantoni,[48] S. B. Beri,[27] G. Bernardi,[17] R. Bernhard,[22] I. Bertram,[42] M. Besançon,[18] R. Beuselinck,[43] V. A. Bezzubov,[38] P. C. Bhat,[48] V. Bhatnagar,[27] G. Blazey,[50] S. Blessing,[47] K. Bloom,[64] A. Boehnlein,[48] D. Boline,[70] E. E. Boos,[37] G. Borissov,[42] T. Bose,[59] A. Brandt,[76] O. Brandt,[23] R. Brock,[62] G. Brooijmans,[68] A. Bross,[48] D. Brown,[17] J. Brown,[17] X. B. Bu,[48] M. Buehler,[79] V. Buescher,[24] V. Bunichev,[37] S. Burdin,[42] T. H. Burnett,[80] C. P. Buszello,[41] B. Calpas,[15] E. Camacho-Pérez,[32] M. A. Carrasco-Lizarraga,[56] B. C. K. Casey,[48] H. Castilla-Valdez,[32] S. Chakrabarti,[70] D. Chakraborty,[50] K. M. Chan,[54] A. Chandra,[78] G. Chen,[56] S. Chevalier-Théry,[18] D. K. Cho,[75] S. W. Cho,[31] S. Choi,[31] B. Choudhary,[28] S. Cihangir,[48] D. Claes,[64] J. Clutter,[56] M. Cooke,[48] W. E. Cooper,[48] M. Corcoran,[78] F. Couderc,[18] M.-C. Cousinou,[15] A. Croc,[18] D. Cutts,[75] A. Das,[45] G. Davies,[43] K. De,[76] S. J. de Jong,[34] E. De La Cruz-Burelo,[32] F. Déliot,[18] M. Demarteau,[48] R. Demina,[69] D. Denisov,[48] S. P. Denisov,[38] S. Desai,[48] C. Deterre,[18] K. DeVaughan,[64] H. T. Diehl,[48] M. Diesburg,[48] A. Dominguez,[64] T. Dorland,[80] A. Dubey,[28] L. V. Dudko,[37] D. Duggan,[65] A. Duperrin,[15] S. Dutt,[27] A. Dyshkant,[50] M. Eads,[64] D. Edmunds,[62] J. Ellison,[46] V. D. Elvira,[48] Y. Enari,[17] H. Evans,[52] A. Evdokimov,[71] V. N. Evdokimov,[38] G. Facini,[60] T. Ferbel,[69] F. Fiedler,[24] F. Filthaut,[34] W. Fisher,[62] H. E. Fisk,[48] M. Fortner,[50] H. Fox,[42] S. Fuess,[48] A. Garcia-Bellido,[69] V. Gavrilov,[36] P. Gay,[13] W. Geng,[15,62] D. Gerbaudo,[66] C. E. Gerber,[49] Y. Gershtein,[65] G. Ginther,[48,69] G. Golovanov,[35] A. Goussiou,[80] P. D. Grannis,[70] S. Greder,[19] H. Greenlee,[48] Z. D. Greenwood,[58] E. M. Gregores,[4] G. Grenier,[20] Ph. Gris,[13] J.-F. Grivaz,[16] A. Grohsjean,[18] S. Grünendahl,[48] M. W. Grünewald,[30] T. Guillemin,[16] F. Guo,[70] G. Gutierrez,[48] P. Gutierrez,[73] A. Haas,[68] S. Hagopian,[47] J. Haley,[60] L. Han,[7] K. Harder,[44] A. Harel,[69] J. M. Hauptman,[55] J. Hays,[43] T. Head,[44] T. Hebbeker,[21] D. Hedin,[50] H. Hegab,[74] A. P. Heinson,[46] U. Heintz,[75] C. Hensel,[23] I. Heredia-De La Cruz,[32] K. Herner,[61] G. Hesketh,[44] M. D. Hildreth,[54] R. Hirosky,[79] T. Hoang,[47] J. D. Hobbs,[70] B. Hoeneisen,[12] M. Hohlfeld,[24] Z. Hubacek,[10,18] N. Huske,[17] V. Hynek,[10] I. Iashvili,[67] R. Illingworth,[48] A. S. Ito,[48] S. Jabeen,[75] M. Jaffré,[16] D. Jamin,[15] A. Jayasinghe,[73] R. Jesik,[43] K. Johns,[45] M. Johnson,[48] D. Johnston,[64] A. Jonckheere,[48] P. Jonsson,[43] J. Joshi,[27] A. W. Jung,[48] A. Juste,[40] K. Kaadze,[57] E. Kajfasz,[15] D. Karmanov,[37] P. A. Kasper,[48] I. Katsanos,[64] R. Kehoe,[77] S. Kermiche,[15] N. Khalatyan,[48] A. Khanov,[74] A. Kharchilava,[67] Y. N. Kharzheev,[35] D. Khatidze,[75] M. H. Kirby,[51] J. M. Kohli,[27] A. V. Kozelov,[38] J. Kraus,[62] S. Kulikov,[38] A. Kumar,[67] A. Kupco,[11] T. Kurča,[20] V. A. Kuzmin,[37] J. Kvita,[9] S. Lammers,[52] G. Landsberg,[75] P. Lebrun,[20] H. S. Lee,[31] S. W. Lee,[55] W. M. Lee,[48] J. Lellouch,[17] L. Li,[46] Q. Z. Li,[48] S. M. Lietti,[5] J. K. Lim,[31] D. Lincoln,[48] J. Linnemann,[62] V. V. Lipaev,[38] R. Lipton,[48] Y. Liu,[7] Z. Liu,[6] A. Lobodenko,[39] M. Lokajicek,[11] R. Lopes de Sa,[70] H. J. Lubatti,[80] R. Luna-Garcia,[32] A. L. Lyon,[48] A. K. A. Maciel,[2] D. Mackin,[78] R. Madar,[18] R. Magaña-Villalba,[32] S. Malik,[64] V. L. Malyshev,[35] Y. Maravin,[57] J. Martínez-Ortega,[32] R. McCarthy,[70] C. L. McGivern,[56] M. M. Meijer,[34] A. Melnitchouk,[63] D. Menezes,[50] P. G. Mercadante,[4] M. Merkin,[37] A. Meyer,[21] J. Meyer,[23] F. Miconi,[19] N. K. Mondal,[29] G. S. Muanza,[15] M. Mulhearn,[79] E. Nagy,[15] M. Naimuddin,[28] M. Narain,[75] R. Nayyar,[28] H. A. Neal,[61] J. P. Negret,[8] P. Neustroev,[39] S. F. Novaes,[5] T. Nunnemann,[25] G. Obrant,[39] J. Orduna,[78] N. Osman,[15] J. Osta,[54] G. J. Otero y Garzón,[1] M. Padilla,[46] A. Pal,[76] N. Parashar,[53] V. Parihar,[75] S. K. Park,[31] J. Parsons,[68] R. Partridge,[75] N. Parua,[52] A. Patwa,[71] B. Penning,[48] M. Perfilov,[37] K. Peters,[44] Y. Peters,[44] K. Petridis,[44] G. Petrillo,[69] P. Pétroff,[16] R. Piegaia,[1] J. Piper,[62] M.-A. Pleier,[71] P. L. M. Podesta-Lerma,[32] V. M. Podstavkov,[48] P. Polozov,[36] A. V. Popov,[38] M. Prewitt,[78] D. Price,[52] N. Prokopenko,[38] S. Protopopescu,[71] J. Qian,[61] A. Quadt,[23] B. Quinn,[63] M. S. Rangel,[2] K. Ranjan,[28] P. N. Ratoff,[42] I. Razumov,[38] P. Renkel,[77] M. Rijssenbeek,[70] I. Ripp-Baudot,[19] F. Rizatdinova,[74] M. Rominsky,[48] A. Ross,[42] C. Royon,[18] P. Rubinov,[48] R. Ruchti,[54] G. Safronov,[36] G. Sajot,[14] P. Salcido,[50] A. Sánchez-Hernández,[32] M. P. Sanders,[25] B. Sanghi,[48] A. S. Santos,[5] G. Savage,[48] L. Sawyer,[58] T. Scanlon,[43] R. D. Schamberger,[70] Y. Scheglov,[39] H. Schellman,[51] T. Schliephake,[26] S. Schlobohm,[80] C. Schwanenberger,[44] R. Schwienhorst,[62] J. Sekaric,[56] H. Severini,[73] E. Shabalina,[23] V. Shary,[18] A. A. Shchukin,[38] R. K. Shivpuri,[28] V. Simak,[10] V. Sirotenko,[48] P. Skubic,[73] P. Slattery,[69] D. Smirnov,[54] K. J. Smith,[67] G. R. Snow,[64] J. Snow,[72] S. Snyder,[71] S. Söldner-Rembold,[44] L. Sonnenschein,[21] K. Soustruznik,[9] J. Stark,[14] V. Stolin,[36] D. A. Stoyanova,[38] M. Strauss,[73] D. Strom,[49] L. Stutte,[48] L. Suter,[44] P. Svoisky,[73] M. Takahashi,[44] A. Tanasijczuk,[1] W. Taylor,[6] M. Titov,[18] V. V. Tokmenin,[35] Y.-T. Tsai,[69] D. Tsybychev,[70] B. Tuchming,[18] C. Tully,[66] L. Uvarov,[39] S. Uvarov,[39] S. Uzunyan,[50] R. Van Kooten,[52] W. M. van Leeuwen,[33] N. Varelas,[49] E. W. Varnes,[45] I. A. Vasilyev,[38] P. Verdier,[20] L. S. Vertogradov,[35] M. Verzocchi,[48] M. Vesterinen,[44] D. Vilanova,[18] P. Vokac,[10] H. D. Wahl,[47]

M. H. L. S. Wang,[69] J. Warchol,[54] G. Watts,[80] M. Wayne,[54] M. Weber,[48] L. Welty-Rieger,[51] A. White,[76] D. Wicke,[26] M. R. J. Williams,[42] G. W. Wilson,[56] M. Wobisch,[58] D. R. Wood,[60] T. R. Wyatt,[44] Y. Xie,[48] C. Xu,[61] S. Yacoob,[51] R. Yamada,[48] W.-C. Yang,[44] T. Yasuda,[48] Y. A. Yatsunenko,[35] Z. Ye,[48] H. Yin,[48] K. Yip,[71] S. W. Youn,[48] J. Yu,[76] S. Zelitch,[79] T. Zhao,[80] B. Zhou,[61] J. Zhu,[61] M. Zielinski,[69] D. Zieminska,[52] and L. Zivkovic[75]

(D0 Collaboration)

[1]*Universidad de Buenos Aires, Buenos Aires, Argentina*
[2]*LAFEX, Centro Brasileiro de Pesquisas Físicas, Rio de Janeiro, Brazil*
[3]*Universidade do Estado do Rio de Janeiro, Rio de Janeiro, Brazil*
[4]*Universidade Federal do ABC, Santo André, Brazil*
[5]*Instituto de Física Teórica, Universidade Estadual Paulista, São Paulo, Brazil*
[6]*Simon Fraser University, Vancouver, British Columbia, and York University, Toronto, Ontario, Canada*
[7]*University of Science and Technology of China, Hefei, People's Republic of China*
[8]*Universidad de los Andes, Bogotá, Colombia*
[9]*Charles University, Faculty of Mathematics and Physics, Center for Particle Physics, Prague, Czech Republic*
[10]*Czech Technical University in Prague, Prague, Czech Republic*
[11]*Center for Particle Physics, Institute of Physics, Academy of Sciences of the Czech Republic, Prague, Czech Republic*
[12]*Universidad San Francisco de Quito, Quito, Ecuador*
[13]*LPC, Université Blaise Pascal, CNRS/IN2P3, Clermont, France*
[14]*LPSC, Université Joseph Fourier Grenoble 1, CNRS/IN2P3, Institut National Polytechnique de Grenoble, Grenoble, France*
[15]*CPPM, Aix-Marseille Université, CNRS/IN2P3, Marseille, France*
[16]*LAL, Université Paris-Sud, CNRS/IN2P3, Orsay, France*
[17]*LPNHE, Universités Paris VI and VII, CNRS/IN2P3, Paris, France*
[18]*CEA, Irfu, SPP, Saclay, France*
[19]*IPHC, Université de Strasbourg, CNRS/IN2P3, Strasbourg, France*
[20]*IPNL, Université Lyon 1, CNRS/IN2P3, Villeurbanne, France and Université de Lyon, Lyon, France*
[21]*III. Physikalisches Institut A, RWTH Aachen University, Aachen, Germany*
[22]*Physikalisches Institut, Universität Freiburg, Freiburg, Germany*
[23]*II. Physikalisches Institut, Georg-August-Universität Göttingen, Göttingen, Germany*
[24]*Institut für Physik, Universität Mainz, Mainz, Germany*
[25]*Ludwig-Maximilians-Universität München, München, Germany*
[26]*Fachbereich Physik, Bergische Universität Wuppertal, Wuppertal, Germany*
[27]*Panjab University, Chandigarh, India*
[28]*Delhi University, Delhi, India*
[29]*Tata Institute of Fundamental Research, Mumbai, India*
[30]*University College Dublin, Dublin, Ireland*
[31]*Korea Detector Laboratory, Korea University, Seoul, Korea*
[32]*CINVESTAV, Mexico City, Mexico*
[33]*FOM-Institute NIKHEF and University of Amsterdam/NIKHEF, Amsterdam, The Netherlands*
[34]*Radboud University Nijmegen/NIKHEF, Nijmegen, The Netherlands*
[35]*Joint Institute for Nuclear Research, Dubna, Russia*
[36]*Institute for Theoretical and Experimental Physics, Moscow, Russia*
[37]*Moscow State University, Moscow, Russia*
[38]*Institute for High Energy Physics, Protvino, Russia*
[39]*Petersburg Nuclear Physics Institute, St. Petersburg, Russia*
[40]*Institució Catalana de Recerca i Estudis Avançats (ICREA) and Institut de Física d'Altes Energies (IFAE), Barcelona, Spain*
[41]*Stockholm University, Stockholm and Uppsala University, Uppsala, Sweden*
[42]*Lancaster University, Lancaster LA1 4YB, United Kingdom*
[43]*Imperial College London, London SW7 2AZ, United Kingdom*
[44]*The University of Manchester, Manchester M13 9PL, United Kingdom*
[45]*University of Arizona, Tucson, Arizona 85721, USA*
[46]*University of California Riverside, Riverside, California 92521, USA*
[47]*Florida State University, Tallahassee, Florida 32306, USA*
[48]*Fermi National Accelerator Laboratory, Batavia, Illinois 60510, USA*
[49]*University of Illinois at Chicago, Chicago, Illinois 60607, USA*
[50]*Northern Illinois University, DeKalb, Illinois 60115, USA*
[51]*Northwestern University, Evanston, Illinois 60208, USA*
[52]*Indiana University, Bloomington, Indiana 47405, USA*

[53]Purdue University Calumet, Hammond, Indiana 46323, USA
[54]University of Notre Dame, Notre Dame, Indiana 46556, USA
[55]Iowa State University, Ames, Iowa 50011, USA
[56]University of Kansas, Lawrence, Kansas 66045, USA
[57]Kansas State University, Manhattan, Kansas 66506, USA
[58]Louisiana Tech University, Ruston, Louisiana 71272, USA
[59]Boston University, Boston, Massachusetts 02215, USA
[60]Northeastern University, Boston, Massachusetts 02115, USA
[61]University of Michigan, Ann Arbor, Michigan 48109, USA
[62]Michigan State University, East Lansing, Michigan 48824, USA
[63]University of Mississippi, University, Mississippi 38677, USA
[64]University of Nebraska, Lincoln, Nebraska 68588, USA
[65]Rutgers University, Piscataway, New Jersey 08855, USA
[66]Princeton University, Princeton, New Jersey 08544, USA
[67]State University of New York, Buffalo, New York 14260, USA
[68]Columbia University, New York, New York 10027, USA
[69]University of Rochester, Rochester, New York 14627, USA
[70]State University of New York, Stony Brook, New York 11794, USA
[71]Brookhaven National Laboratory, Upton, New York 11973, USA
[72]Langston University, Langston, Oklahoma 73050, USA
[73]University of Oklahoma, Norman, Oklahoma 73019, USA
[74]Oklahoma State University, Stillwater, Oklahoma 74078, USA
[75]Brown University, Providence, Rhode Island 02912, USA
[76]University of Texas, Arlington, Texas 76019, USA
[77]Southern Methodist University, Dallas, Texas 75275, USA
[78]Rice University, Houston, Texas 77005, USA
[79]University of Virginia, Charlottesville, Virginia 22901, USA
[80]University of Washington, Seattle, Washington 98195, USA

(Received 31 May 2011; published 9 August 2011)

We report a measurement of the mass of the top quark in lepton + jets final states of $p\bar{p} \rightarrow t\bar{t}$ data corresponding to 2.6 fb^{-1} of integrated luminosity collected by the D0 experiment at the Fermilab Tevatron Collider. A matrix-element method is developed that combines an *in situ* jet energy calibration with our standard jet energy scale derived from studies of γ + jet and dijet events. We then implement a flavor-dependent jet-response correction through a novel approach. This method is used to measure a top-quark mass of $m_t = 176.01 \pm 1.64$ GeV. Combining this result with our previous result obtained on an independent data set, we measure a top-quark mass of $m_t = 174.94 \pm 1.49$ GeV for a total integrated luminosity of 3.6 fb^{-1}.

DOI: 10.1103/PhysRevD.84.032004 PACS numbers: 14.65.Ha

I. INTRODUCTION

The observation of the top quark in 1995 [1,2] confirmed the existence of the six quarks in three generations of fermions expected in the standard model (SM) of particle interactions. Because of its mass, the lifetime of the top quark is much shorter than the time scale of hadronization. The top quark can therefore decay before interacting, making it the only quark whose characteristics can be studied in isolation. The large mass of the top quark (m_t), corresponding to a Yukawa coupling to the Higgs boson equal to 1 within the current uncertainties, suggests a special role for the top quark in the breaking of electroweak symmetry. It is therefore not surprising that the precise determination of the mass of the top quark has received great attention. The interest in the top-quark mass also arises from the constraint imposed on the mass of the Higgs boson, m_H, from the relationship among the values of m_t, m_H, and the SM radiative corrections to the mass of the W boson [3]. A precise measurement of m_t also provides a useful constraint on contributions from physics beyond the standard model [4].

The statistical uncertainty on the world average value of m_t is 0.3%, and the accuracy of the measurement of m_t is now dominated by systematic uncertainties [5]. The main systematic contributions arise from uncertainties on the jet energy calibration and on the Monte Carlo (MC) simulation of $t\bar{t}$ events.

We present a new measurement of the mass of the top quark based on 2.6 fb^{-1} of integrated luminosity from $p\bar{p}$ collisions at $\sqrt{s} = 1.96$ TeV, collected with the D0 detector at the Fermilab Tevatron Collider. The analysis focuses on $t\bar{t}$ events identified in lepton + jets (ℓ + jets) final states (with ℓ representing either an electron or a muon) [6], in which the top and antitop quark are assumed to decay into

a W boson and b quark [7], with one of the W bosons in the $W^+W^-b\bar{b}$ final system decaying via $W \to \ell\nu$ into a lepton and neutrino and the other via $W \to q\bar{q}'$ into two quarks, and all four quarks ($q\bar{q}'b\bar{b}$) into jets. Such events are characterized by an isolated electron or muon with large transverse momentum (p_T), an undetected neutrino that causes a large imbalance in transverse momentum, and four high-p_T jets. In selecting candidate events, we exploit this distinct signature, which helps distinguish these events from background.

Compared to the previous measurement based on data corresponding to 1 fb^{-1} of integrated luminosity [8], we use a larger data set and an improved evaluation of systematic uncertainties. The analysis uses the same matrix element (ME) analysis technique, with an *in situ* jet energy calibration based on constraining the invariant mass of the two jets from the decay of the W boson to the world average value of $M_W = 80.4$ GeV [9]. As in the previous measurement, the standard jet energy scale (JES), derived from γ + jet and dijet data samples, is used as an additional constraint and implemented through a Gaussian prior on its absolute value and uncertainty. A major improvement in this new measurement is the significant reduction of the uncertainty associated with the modeling of differences in the calorimeter response to b-quark and light-quark jets originating from the introduction of a new flavor-dependent jet energy response correction.

This measurement, like all direct measurements of m_t, relies on MC $t\bar{t}$ events for absolute calibration. It is therefore important to understand the precise definition of the input mass $m_t^{\rm gen}$ in MC $t\bar{t}$ event generators, such as ALPGEN [10] and PYTHIA [11], used to calibrate the direct measurements. Although $m_t^{\rm gen}$ is not well defined in leading order (LO) generators that use parton showers to model higher-order effects and hadronization, it has been argued that $m_t^{\rm gen}$ should be viewed as being close to the pole mass [12]. In Ref. [13], the D0 Collaboration has extracted m_t from a comparison of the measured $t\bar{t}$ production cross section with predictions from higher-order quantum chromodynamics (QCD) by equating $m_t^{\rm gen}$ both with the pole mass ($m_t^{\rm pole}$) and with the $\overline{\rm MS}$ mass ($m_t^{\overline{\rm MS}}$). The extracted m_t, under the assumption $m_t^{\rm gen} \equiv m_t^{\rm pole}$, is found to agree with the average value of m_t from the Tevatron, while the m_t extracted assuming $m_t^{\rm gen} \equiv m_t^{\overline{\rm MS}}$ is found to be different from the average value of m_t. These results favor the pole mass interpretation of $m_t^{\rm gen}$.

This paper is arranged as follows. A brief description of the D0 detector is given in Sec. II, which is followed by a discussion of the selection and reconstruction of the physical objects in this analysis in Sec. III. Section IV summarizes the MC samples used to simulate the events of interest, and Sec. V discusses the technique used to extract the value of m_t. This is followed by a description of the calibration of the response of the analysis method in Sec. VI and a discussion of the flavor-dependent jet-response correction used to bring the simulation of the calorimeter response to jets into agreement with data in Sec. VII. The result of the calibration is applied to the data in Sec. VIII, where the measured value of m_t and its statistical uncertainty are also presented. Section IX describes the evaluation of systematic uncertainties and the final result is given in Sec. X. We combine this new measurement in Sec. XI with an updated version of that from Ref. [8] in which the flavor-dependent jet-response correction mentioned above has been applied and the systematic uncertainties have been updated.

II. THE D0 DETECTOR

The D0 detector consists primarily of a magnetic central tracking system, calorimetry, and a muon system. The central tracking system comprises a silicon microstrip tracker (SMT) and a central fiber tracker (CFT), both located within a 1.9 T superconducting solenoidal magnet [14]. The SMT [15] has $\approx 800,000$ individual strips, with typical pitch of 50–80 μm, and a design optimized for track and vertex finding at $|\eta| < 2.5$, where the pseudorapidity $\eta = -\ln[\tan(\theta/2)]$, and is the polar angle with respect to the proton beam direction relative to the center of the detector. The system has a six-barrel longitudinal structure, each with a set of four layers arranged axially around the beam pipe and interspersed with 16 radial disks. In 2006, a fifth layer, referred to as Layer 0, was installed close to the beam pipe [16,17]. The CFT has eight thin coaxial barrels, each supporting two doublets of overlapping scintillating fibers of 0.835 mm diameter, one doublet being parallel to the collision axis and the other alternating by $\pm 3°$ relative to the axis. Light signals are transferred via clear fibers to solid-state photon counters (VLPCs) that have 80% quantum efficiency.

Central and forward preshower detectors, located just outside of the superconducting coil (in front of the calorimetry), are constructed of several layers of extruded triangular scintillator strips that are read out using wavelength-shifting fibers and the VLPC. These detectors provide initial sampling of electromagnetic showers, and thereby help distinguish incident photons from electrons. The next layer of detection involves three liquidargon/uranium calorimeters: a central section (CC) covering $|\eta|$ up to ≈ 1.1 and two end calorimeters (EC) that extend coverage to $|\eta| \approx 4.2$, all housed in separate cryostats. The electromagnetic (EM) section of the calorimeter is segmented into four layers, with transverse segmentation of the cells in pseudorapidity and azimuth of $\Delta\eta \times \Delta\phi = 0.1 \times 0.1$, except for the third layer, where the segmentation is 0.05×0.05. The hadronic portion of the calorimeter is located after the EM sections, and consists of fine hadron-sampling layers, followed by more coarse hadronic layers. In addition, scintillators between the CC and EC cryostats provide sampling of developing showers for $1.1 < |\eta| < 1.4$. A muon system [18] is located beyond

the calorimetry and consists of a layer of tracking detectors and scintillation trigger counters before 1.9 T toroids, followed by two similar layers after the toroids. Tracking for $|\eta| < 1$ relies on 10 cm wide drift tubes, while 1 cm mini-drift tubes are used for $1 < |\eta| < 2$.

Luminosity is measured using plastic scintillator arrays located in front of the EC cryostats, covering $2.7 < |\eta| < 4.4$. The trigger and data acquisition systems are designed to accommodate the high instantaneous luminosities of the Tevatron [14,19]. Based on preliminary information from tracking, calorimetry, and muon systems, the output of the first level of the trigger is used to limit the rate for accepted events to 2 kHz. At the next trigger stage, with more refined information, the rate is reduced further to 1 kHz. These first two levels of triggering rely mainly on hardware and firmware. The third and final level of the trigger, with access to all of the event information, uses software algorithms and a computing farm and reduces the output rate to 100 Hz, which is written to tape.

III. OBJECT RECONSTRUCTION AND EVENT SELECTION

In the following sections, we summarize how the physical objects in data and MC events are reconstructed from information in the detector and the criteria applied to these objects to select the ℓ + jets $t\bar{t}$ candidate events.

A. Object reconstruction

This section describes the reconstruction of electrons, muons, missing transverse momentum, and jets, and the identification of b jets.

1. Identification of electrons

Electron candidates are defined by narrow clusters of energy deposited in towers of the electromagnetic calorimeter located within a cone of radius $\mathcal{R} = \sqrt{(\Delta\eta)^2 + (\Delta\phi)^2} = 0.2$, where $\Delta\eta$ is the pseudorapidity and $\Delta\phi$ is the azimuthal angle of each cluster relative to the seed cluster. At least 90% of the total energy measured within this cone is required to be located within the electromagnetic section to be consistent with expectations for electromagnetic showers. Isolation from energy deposited by hadrons is imposed by requiring $(E_{\text{tot}} - E_{\text{EM}})/E_{\text{EM}} < 0.15$, where E_{tot} (E_{EM}) is the total (electromagnetic) energy in a cone of radius $\mathcal{R} = 0.4$ ($\mathcal{R} = 0.2$). Candidate electrons are required to have longitudinal and transverse shower profiles compatible with those of electromagnetic showers and to be spatially matched to a track reconstructed in the central tracking system. Electron candidates meeting these criteria are referred to as *loose* electrons. Finally, (i) the value of a multivariable likelihood discriminant based on tracking system and calorimeter information is required to be consistent with that for an electron, and (ii) a neural network, trained using information from the tracking system, calorimeter, and central preshower detector is used to further reject background from jets misidentified as electrons. Electron candidates meeting these criteria are referred to as *tight* electrons, and are those used to obtain the final selection.

2. Identification of muons

Muons are identified by requiring a minimum number of wire and scintillator hits on both sides of the toroidal magnets in the muon detector [18]. Cosmic ray background is rejected by requiring scintillator signals consistent in time with muons originating from the $p\bar{p}$ collision. Tracks in the muon system are required to match a reconstructed track in the central tracker having a small impact parameter (par.) with respect to the $p\bar{p}$ interaction vertex (PV) to reject muons from cosmic rays and decays in flight of kaons and pions. Muon candidates must also be isolated from jets with $p_T > 15$ GeV by requiring a separation in $\eta - \phi$ space between the muon and jet of $\Delta\mathcal{R}(\mu, \text{jet}) > 0.5$ [20]. Candidates satisfying these requirements are referred to as *loosely isolated* muons. The following two variables are used to impose additional isolation requirements: $E_{\text{halo}}^{\text{scaled}}$ is defined as the ratio of calorimeter energy within an annulus of $0.1 < \mathcal{R} < 0.4$ around the muon direction to the p_T of the muon; $p_{T,\text{cone}}^{\text{scaled}}$ is defined as the ratio of the total p_T of all tracks within a cone of $\mathcal{R} = 0.5$, excluding the muon, to the p_T of the muon. Muon candidates meeting all the requirements above that satisfy $E_{\text{halo}}^{\text{scaled}} < 0.12$ and $p_{T,\text{cone}}^{\text{scaled}} < 0.12$ are referred to as *veto* muons. Further tightening these requirements to $E_{\text{halo}}^{\text{scaled}} < 0.08$ and $p_{T,\text{cone}}^{\text{scaled}} < 0.06$ selects candidates referred to as *tightly isolated* muons.

3. Measurement of the imbalance in transverse momentum

We use the conservation of momentum to measure the momentum imbalance in the transverse plane ($\not{p}_T$). From that, we infer the presence of the neutrino. The $\not{p}_T$ is determined from the vector sum of the energies of all cells in the electromagnetic and hadronic calorimeters. Subsequent energy corrections applied to reconstructed objects such as jets and muons are also propagated to the missing transverse momentum.

4. Identification of jets

Jet candidates are reconstructed using the iterative midpoint cone algorithm with a cone radius of $\mathcal{R} = 0.5$ [21]. Only calorimeter cells with energies that are 2.5 standard deviations above the mean of the noise distribution are considered in the reconstruction. Isolated cells with energies less than 4 standard deviations above the mean of the noise distribution are also discarded. Among the jet candidates with $p_T > 8$ GeV, the following selection criteria are

imposed. The electromagnetic fraction of the jet energy is required to be below 0.95 to reject electrons and above 0.05 to suppress jets dominated by noise from the hadronic part of the calorimeter. Jets with a large fraction of their energy deposited in the coarse hadronic layers of the calorimeter are rejected to suppress jets dominated by noise typical for those layers. To minimize background from jet candidates arising from noise in the precision readout of the calorimeter, confirmation from the readout system of the first level trigger is required for reconstructed jets. Jets matched to loose electrons with $p_T > 20$ GeV and $\Delta\mathcal{R}(e, \text{jet}) < 0.5$ [20] are also rejected. Energies of jets containing muons are corrected with the measured muon momentum after accounting for the typical energy deposited by a minimum ionizing particle.

The energy of a reconstructed jet is corrected, on average, to that of a *particle jet* [22] containing the final-state particles within a cone of radius $\mathcal{R} = 0.5$ corresponding to the reconstructed jet. The first step involves the subtraction of the offset energy due to calorimeter noise and contributions from previous and following beam crossings and multiple interactions within the same beam crossing. This is followed by an absolute response correction determined from γ + jet events and a relative η-dependent correction based on γ + jet and dijet events. Finally, a showering correction is applied to account for the lateral leakage of energy across the jet cone boundary.

5. Identification of b jets

The lifetime of the b quark, unlike that of the top quark, is far longer than the time-scale for hadronization. This means that, during QCD evolution, the b quark can form short lived b hadrons that travel $\gtrsim 1$ mm before decaying through the weak interaction. We identify the b jets among the candidates satisfying the jet selection criteria described in the previous section by using a neural network (NN) b-tagging algorithm that selects jets with displaced vertices and tracks relative to the PV [23]. The NN tagger is based on nine input variables that can be separated into two categories. The first category is related to the reconstructed secondary vertex and includes the vertex quality, the number of associated tracks, the invariant mass of the vertex, the number of secondary vertices reconstructed within the jet, the spatial separation between the jet axis and the position vector of the secondary vertex relative to the PV, and the length of the flight path projected on the transverse plane divided by its uncertainty (which provides a measure of the decay length significance in terms of standard deviations). The second category relies only on the characteristics of the tracks within the jets such as impact parameters, transverse momentum, and track quality. The b-jet candidates are also required to have at least two good quality tracks originating from the PV. The tagging efficiency for b jets is $\approx 65\%$ for a misidentification rate of $\approx 3\%$ for u, d, s quark, or gluon jets [24].

B. Event selection

The data sample used in this analysis was collected with the D0 detector at the Tevatron between June 2006 and June 2008, and corresponds to an integrated luminosity of 2.6 fb^{-1}. The selected events must satisfy a single-lepton trigger, requiring a high p_T electron or muon, or a lepton + jets trigger, requiring a lower-p_T electron or muon accompanied by a jet. Events are required to have at least one PV with >2 tracks reconstructed within the fiducial region of the SMT. We require exactly four jets with $|\eta| < 2.5$, with the leading (highest p_T) jet having $p_T > 40$ GeV and the other jets $p_T > 20$ GeV. Leptons are required to originate from within 1 cm of the PV in the coordinate along the beam line. Exactly one tight electron (or tightly isolated muon) with $p_T > 20$ GeV and $|\eta| < 1.1$ ($|\eta| < 2$) is also required. Electron + jets events containing a second tight electron with $p_T > 15$ GeV and $|\eta| < 2.5$ or a veto muon with $p_T > 15$ GeV and $|\eta| < 2$ are rejected. Muon + jets events containing a second muon that is a veto muon with $p_T > 15$ GeV and $|\eta| < 2$ or a tight electron with $p_T > 15$ GeV and $|\eta| < 2.5$ are rejected. The missing transverse momentum is required to satisfy $\not{p}_T > 20$ GeV ($\not{p}_T > 25$ GeV) for e + jets (μ + jets) events. Multijet background, typically arising from mismeasurement of lepton or jet energies, is suppressed by requiring a minimal azimuthal separation between the lepton direction and the $\not{p}_T$ vector with $\Delta\phi(e, \not{p}_T) > 0.7\pi - 0.045 \cdot \not{p}_T$ for electrons and $\Delta\phi(\mu, \not{p}_T) > 2.1 - 0.035 \cdot \not{p}_T$ for muons, with $\not{p}_T$ in GeV and $\Delta\phi(\ell, \not{p}_T) = |\phi_\ell - \phi_{\not{p}_T}|$. Any μ + jets events with an invariant mass, $m_{\mu\mu}$, of the isolated muon and a second muon (with $p_T >$ 15 GeV and even lower quality requirements than a loosely isolated muon) of $70 < m_{\mu\mu} < 110$ GeV are rejected in order to suppress $Z(\rightarrow \mu\mu)$ + jets events. The data sample satisfying the above criteria consists of 825 e + jets and 737 μ + jets events. We further require at least one jet to be identified as a b jet, which yields the final data samples of 312 e + jets and 303 μ + jets events.

IV. MONTE CARLO SAMPLES

The MC events used to model the $t\bar{t}$ signal and the W + jets background needed for the calibration of the measurement (described in Sec. VI) are generated using ALPGEN [10] to simulate the hard-scattering process and PYTHIA [11] to simulate hadronization and shower evolution. The MLM matching scheme [25] is employed to avoid overlaps between components of the event belonging to the hard process, implemented through a matrix element, and parton evolution (showering) into jets. The W + jets background samples are divided into two categories: (i) $W + lp$ and (ii) $W + (c\bar{c}, lp)$ and $W + (b\bar{b}, lp)$, where lp (light partons) denotes u, d, s quarks, or gluons. Although the individual processes are produced with ALPGEN which is a LO generator, the relative contributions

between the two categories are determined using next-to-leading order (NLO) calculations, with next-to-leading logarithmic (NLL) corrections based on the MCFM MC generator [26]. The MC samples used to derive jet transfer functions that correlate jet energies with those of partons in the $t\bar{t}$ events (described in Sec. V B 1) are generated using PYTHIA to simulate both the hard-scattering process and the subsequent hadronization and shower evolution for the events. All MC samples are generated with CTEQ6L1 parton distribution functions (PDFs) [27] and passed through a full GEANT3-based [28] simulation of the D0 detector. To simulate the effects from additional $p\bar{p}$ interactions, events with no trigger requirements selected from random $p\bar{p}$ crossings in the collider data having the same instantaneous luminosity profile as the data are overlayed on the fully simulated MC events. This is then followed by the same reconstruction and analysis chain as applied to data.

V. METHOD OF ANALYSIS

The top-quark mass is measured using all kinematic information with a likelihood technique based on probability densities (PDs) constructed, for each individual event, from matrix elements of the processes contributing to the observed final state. This analysis technique, referred to as the matrix-element (ME) method [29], is described below.

A. Matrix-element method

If the processes contributing to an observed event do not interfere, the total PD for observing a given event is the sum of all contributing probabilities for that specific final state. Assuming that $t\bar{t}$ and W + jets production are the only two contributions, the PD for observing each event is given in terms of the top-quark mass m_t, the jet energy scale factor k_{JES} dividing the energies of all jets, and the fractions of $t\bar{t}$ signal (f) and of W + jets background ($1 - f$) in the data by

$$P_{\mathrm{evt}} = A(x)[fP_{\mathrm{sig}}(x; m_{\mathrm{t}}, k_{\mathrm{JES}}) + (1 - f)P_{\mathrm{bkg}}(x; k_{\mathrm{JES}})], \tag{1}$$

where x represents the measured jet and lepton energies and angles; $A(x)$, which depends only on x, accounts for the geometrical acceptance and efficiencies; and P_{sig} and P_{bkg} are the PDs for $t\bar{t}$ and W + jets production, respectively. For events satisfying $P_{\mathrm{bkg}} \gg P_{\mathrm{sig}}$, the relative contribution of P_{sig} to P_{evt} is negligible and has minimal influence on the determination of m_t. Multijet events satisfy this condition and can therefore be represented by P_{bkg}, as the event kinematics are far closer to W +jets than to $t\bar{t}$ production.

Because of the finite detector resolution and the hadronization process, the measured set x for the observed events will not, in general, be identical to the corresponding set y of the original final-state partons and the relationship between x and y is described by a transfer function. In addition, the initial partons carry momenta q_1 and q_2 in the colliding p and $\bar{p}$. To account for this complication, P_{sig} and P_{bkg} must be integrated over all parton states contributing to the observed set x. This involves a convolution of the partonic differential cross section $d\sigma(y)$ with the PDFs and a transfer function $W(x, y; k_{\mathrm{JES}})$ that relates x and y:

$$P(x, \alpha) = \frac{1}{\sigma(\alpha)} \int \sum_{\mathrm{flavors}} d\sigma(y, \alpha) dq_1 dq_2 f(q_1) \times f(q_2) W(x, y; k_{\mathrm{JES}}), \tag{2}$$

where α represents the parameters to be determined in the analysis, the sum runs over all possible initial-state parton flavors, and $f(q_i)$ are CTEQ6L1 PDFs for finding a parton of a given flavor and longitudinal momentum fraction q_i in the p or $\bar{p}$. Detector resolution is taken into account in $W(x, y; k_{\mathrm{JES}})$, representing the probability density for the measured set x to have arisen from the partonic set y. Dividing by the total observed cross section for the process, $\sigma(\alpha)$, ensures $P(x; \alpha)$ is normalized to unity.

The differential cross section term for P_{sig} is calculated using the LO ME of the quark-antiquark annihilation process ($\mathcal{M}_{t\bar{t}}$). A total of 24 integration variables are associated with the two initial-state partons and the six particles in the final state. Since the angles for the four jets and the charged lepton are sufficiently well measured, the angular resolution terms in $W(x, y; k_{\mathrm{JES}})$ can be approximated by Dirac δ functions. Integrating over these and four more δ functions that impose energy-momentum conservation leaves 10 integrals to evaluate the probability density that represents the $t\bar{t}$ production probability for a given m_t and k_{JES} [30]:

$$P_{\mathrm{sig}} = \frac{1}{\sigma_{\mathrm{obs}}^{t\bar{t}}} \sum_{i=1}^{24} w_i \int d\rho dm_1^2 dM_1^2 dm_2^2 dM_2^2 d\rho_\ell dq_1^{\mathrm{x}} dq_1^{\mathrm{y}} dq_2^{\mathrm{x}} dq_2^{\mathrm{y}} \sum_{\mathrm{flavors},\nu} |\mathcal{M}_{t\bar{t}}|^2 \frac{f'(q_1) f'(q_2)}{\sqrt{(\eta_{\alpha\beta} q_1^\alpha q_2^\beta)^2 - m_{q_1}^2 m_{q_2}^2}} \Phi_6 W(x, y; k_{\mathrm{JES}}), \tag{3}$$

where, in addition to the CTEQ6L1 PDF given by $f(q_i)$, the $f'(q_i)$ also include parameterizations of the probability distributions for the transverse momenta $q_i^{\mathrm{x,y}}$ of the initial-state partons in PYTHIA [11]. The masses of the initial-state partons are given by m_{q_i}, and Φ_6 includes the 6-body phase-space factor and other constants. The first sum is over all 24 jet permutations, each carrying a weight w_i, which is the product of four jet weights. The weight for

a b-tagged jet with a given p_T and η is the average tagging efficiency $\epsilon_\alpha(p_T, \eta)$ for a given parton hypothesis $\alpha(= b, c,$ light$q$, or gluon). The weight for a jet that is not b-tagged is $1 - \epsilon_\alpha(p_T, \eta)$. The second sum includes up to eight solutions for neutrino kinematics and conservation of transverse momentum used to calculate the transverse momentum of the neutrino. The parameter ρ represents the fraction of the energy carried by one of the quarks from the $W \to q\bar{q}'$ decay. The masses of the two W bosons (M_1, M_2) and of the pair of top quarks (m_1, m_2) are chosen as integration variables because of computational efficiency related to the four Breit-Wigner mass terms that make the ME negligible everywhere except at the mass peaks. The energy (the curvature $1/p_T$) of the electron (muon) is defined by ρ_ℓ. The integration over q_i involves only transverse components. $W(x, y; k_{\rm JES})$ is the product of five terms for the four jets and one charged lepton, described below. The normalization $\sigma^{t\bar{t}}_{\rm obs} = \int A(x) P_{\rm sig} dx = \sigma^{t\bar{t}}(m_t) \times \langle A(m_t, k_{\rm JES})\rangle$ is calculated from the product of the total cross section corresponding to the ME used and the mean acceptance for events whose dependencies on m_t and $k_{\rm JES}$ are determined from MC events. The mean acceptance is shown in Fig. 1 as a function of m_t for different values of $k_{\rm JES}$.

The differential cross section in $P_{\rm bkg}$ is calculated using the $W + 4$ jets matrix elements from the VECBOS [31] MC program. The initial-state partons are assumed to have no transverse momenta. The integration is performed over the W boson mass, the energy $(1/p_T)$ of the electron (muon), and the energies of the four partons producing the jets, summing over the 24 jet permutations and all neutrino solutions.

The top-quark mass is extracted from n events with a measured set of variables $\tilde{x} = (x_1, x_2, \ldots, x_n)$ through a likelihood function for individual event probabilities $P_{\rm evt}$ according to

$$L(\tilde{x}; m_t, k_{\rm JES}, f) = \prod_{i=1}^{n} P_{\rm evt}(x_i; m_t, k_{\rm JES}, f). \qquad (4)$$

For every assumed pair of $(m_t, k_{\rm JES})$ values, the value of $f^{\rm best}$ that maximizes the likelihood is determined. To obtain

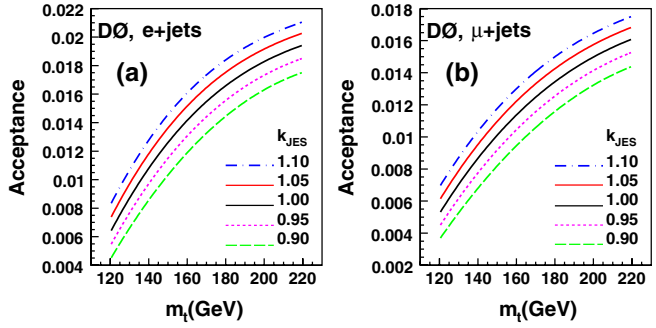

FIG. 1 (color online). The mean acceptance as a function of m_t and $k_{\rm JES}$ for the (a) e + jets and (b) μ + jets channels.

the best estimate of m_t and $k_{\rm JES}$, the two-dimensional likelihood

$$L(\tilde{x}; m_t, k_{\rm JES}) = L[\tilde{x}; m_t, k_{\rm JES}, f^{\rm best}(m_t, k_{\rm JES})] \qquad (5)$$

is projected onto the m_t and $k_{\rm JES}$ axes according to

$$L(\tilde{x}; m_t) = \int L(\tilde{x}; m_t, k_{\rm JES}) G(k_{\rm JES}) dk_{\rm JES} \qquad (6)$$

and

$$L(\tilde{x}; k_{\rm JES}) = \int L(\tilde{x}; m_t, k_{\rm JES}) dm_t, \qquad (7)$$

using Simpson's rule [32], where the prior probability distribution $G(k_{\rm JES})$ is a Gaussian function centered at $k_{\rm JES} = 1$ with standard deviation (sd) 0.02 determined from the mean of the fractional uncertainty of the standard jet energy scale corrections applied to all jets in the MC samples used in this analysis. The best estimates and the uncertainties on the mass of the top quark and the jet energy scale are then extracted using the mean and the rms of $L(\tilde{x}; m_t)$ and $L(\tilde{x}; k_{\rm JES})$, respectively. The mean is calculated from $\bar{\alpha} = \int \alpha L(\tilde{x}; \alpha) d\alpha / \int L(\tilde{x}; \alpha) d\alpha$ and the rms from $\sigma^2(\alpha) = \int (\alpha - \bar{\alpha})^2 L(\tilde{x}; \alpha) d\alpha / \int L(\tilde{x}; \alpha) d\alpha$, where α corresponds to m_t or $k_{\rm JES}$, also using Simpson's rule.

The fit parameter $k_{\rm JES}$, associated with the *in situ* jet energy calibration, has the effect of rescaling the energies of all the jets and thereby the 2-jet invariant mass of the hadronically decaying W boson, with the jet energy scale factor $k_{\rm JES}$. The presence of the Breit-Wigner mass term associated with the hadronically decaying W boson in the ME of Eq. (3) maximizes the likelihood in Eq. (4) when the 2-jet invariant mass coincides with the Breit-Wigner pole fixed at the world average of $M_W = 80.4$ GeV [9]. The additional constraint to the standard scale derived from γ + jet and dijet samples is applied through the prior probability distribution $G(k_{\rm JES})$ in Eq. (6).

B. Detector resolution

In this section, we describe the parameterizations for the jet and electron energy and muon p_T resolutions used in the transfer function $W(x, y; k_{\rm JES})$ which is the product of four jet transfer functions for a given jet permutation and an electron or muon transfer function.

1. Parameterization of jet energy resolution

The transfer function for jets, $W_{\rm jet}(E_x, E_y; k_{\rm JES})$, represents the probability that a measured jet energy E_x in the detector corresponds to a parent quark of energy E_y. It is parameterized in terms of a double Gaussian function whose means and widths are dependent on E_y. For the case $k_{\rm JES} = 1$, it is given by

TABLE I. Transfer function parameters for light quarks (a_i in GeV).

	Light-quark jets			
Par.	$\lvert\eta\rvert < 0.5$	$0.5 < \lvert\eta\rvert < 1$	$1 < \lvert\eta\rvert < 1.5$	$1.5 < \lvert\eta\rvert < 2.5$
a_1	-2.74×10^{0}	-8.02×10^{-1}	1.69×10^{-1}	1.52×10^{1}
b_1	1.67×10^{-2}	-3.59×10^{-3}	1.32×10^{1}	-2.17×10^{-1}
a_2	5.44×10^{0}	5.40×10^{0}	-3.26×10^{-1}	3.34×10^{0}
b_2	6.29×10^{-2}	8.46×10^{-2}	6.97×10^{0}	1.45×10^{-1}
b_3	4.30×10^{-4}	4.80×10^{-4}	2.52×10^{-2}	4.06×10^{-3}
a_4	1.54×10^{1}	2.00×10^{1}	4.71×10^{0}	1.72×10^{1}
b_4	-2.12×10^{-1}	-2.38×10^{-1}	-8.37×10^{-3}	-3.69×10^{-2}
a_5	1.77×10^{1}	-2.38×10^{-1}	1.03×10^{1}	1.75×10^{1}
b_5	1.96×10^{-1}	1.89×10^{1}	6.42×10^{-2}	5.34×10^{-2}

$$W_{\text{jet}}(E_x, E_y; k_{\text{JES}} = 1) = \frac{1}{\sqrt{2\pi}(p_2 + p_3 p_5)}\left[e^{-([(E_x - E_y) - p_1]^2)/2p_2^2} + p_3 e^{-([(E_x - E_y) - p_4]^2)/2p_5^2}\right], \tag{8}$$

where the p_i are functions of the quark energy for quark i and are parameterized as linear functions of the E_y:

$$p_i = a_i + E_y \cdot b_i. \tag{9}$$

The parameters a_i and b_i are determined from fully simulated $t\bar{t}$ events, following all jet energy corrections and smearing to match resolutions in data. These events are generated with PYTHIA at nine values of the top-quark mass ranging from 155 to 195 GeV in 5 GeV intervals. The parton and jet energies are used in an unbinned likelihood fit that minimizes the product of the W_{jet} terms for each event with respect to a_i and b_i. A different set of parameters is derived (i) for three varieties of quarks: light quarks (u, d, s, c), b quarks with a soft muon tag in the jet [33], and all other b quarks, and (ii) for four η regions: $\lvert\eta\rvert < 0.5$, $0.5 < \lvert\eta\rvert < 1.0$, $1.0 < \lvert\eta\rvert < 1.5$, and $1.5 < \lvert\eta\rvert < 2.5$, to minimize possible effects due to nonuniform calorimeter response. The values for these parameters are shown in Tables I and II for light-quark and b-quark jets, respectively. Figure 2 illustrates the transfer functions for light-quark jets as a function of E_x for different values of E_y. In Fig. 3, we compare the 2-jet and 3-jet invariant mass distributions for two types of PYTHIA $t\bar{t}$ ℓ + jets events: (i) parton-level events with jet energies smeared using the transfer functions and (ii) fully simulated events where all four reconstructed jets are matched to partons with $\Delta\mathcal{R}(\text{parton, jet}) < 0.5$. The 2-jet (3-jet) invariant masses are calculated using the two light-quark jets (all three jets) from the hadronic branch of the $t\bar{t}$ ℓ + jets events and correspond to the W boson (top-quark) mass. The overlaid distributions in Fig. 3 indicate that the jet transfer functions describe the jet resolutions well.

For $k_{\text{JES}} \neq 1$, the jet transfer function is changed to

$$W_{\text{jet}}(E_x, E_y; k_{\text{JES}}) = \frac{W_{\text{jet}}(\frac{E_x}{k_{\text{JES}}}, E_y; 1)}{k_{\text{JES}}}, \tag{10}$$

where the k_{JES} factor in the denominator preserves the normalization $\int W_{\text{jet}}(E_x, E_y; k_{\text{JES}})dE_x = 1$.

TABLE II. Transfer function parameters for b-quark jets without and with a muon within the jet cone (a_i in GeV).

b-quark jets without a muon within the jet cone					b-quark jets with a muon within the jet cone				
Par.	$\lvert\eta\rvert < 0.5$	$0.5 < \lvert\eta\rvert < 1$	$1 < \lvert\eta\rvert < 1.5$	$1.5 < \lvert\eta\rvert < 2.5$	Par.	$\lvert\eta\rvert < 0.5$	$0.5 < \lvert\eta\rvert < 1$	$1 < \lvert\eta\rvert < 1.5$	$1.5 < \lvert\eta\rvert < 2.5$
a_1	3.30×10^{0}	5.38×10^{0}	2.85×10^{0}	1.38×10^{1}	a_1	6.37×10^{0}	6.31×10^{0}	8.00×10^{0}	1.65×10^{1}
b_1	-2.13×10^{-1}	-2.26×10^{-1}	-1.85×10^{-1}	-2.90×10^{-1}	b_1	-1.46×10^{-1}	-1.40×10^{-1}	-1.39×10^{-1}	-1.91×10^{-1}
a_2	5.02×10^{0}	5.08×10^{0}	9.78×10^{-1}	3.86×10^{0}	a_2	2.53×10^{0}	3.89×10^{0}	8.54×10^{0}	4.88×10^{0}
b_2	1.73×10^{-1}	1.77×10^{-1}	1.83×10^{-1}	1.36×10^{-1}	b_2	1.43×10^{-1}	1.37×10^{-1}	1.28×10^{-1}	1.43×10^{-1}
b_3	3.48×10^{-2}	2.49×10^{-2}	6.69×10^{-3}	7.52×10^{-3}	b_3	3.90×10^{-4}	3.40×10^{-4}	1.90×10^{-4}	1.20×10^{-4}
a_4	-6.68×10^{0}	-6.56×10^{0}	8.54×10^{-1}	5.59×10^{0}	a_4	2.80×10^{1}	1.52×10^{1}	7.89×10^{1}	4.73×10^{1}
b_4	2.38×10^{-2}	1.91×10^{-2}	-2.83×10^{-2}	-4.54×10^{-2}	b_4	-3.87×10^{-1}	-9.74×10^{-2}	2.22×10^{-1}	5.21×10^{-2}
a_5	5.06×10^{0}	4.36×10^{0}	1.38×10^{1}	1.50×10^{1}	a_5	1.80×10^{1}	2.32×10^{1}	2.80×10^{1}	2.83×10^{1}
b_5	4.71×10^{-2}	6.99×10^{-2}	6.04×10^{-2}	7.60×10^{-2}	b_5	1.30×10^{-1}	2.91×10^{-2}	-2.87×10^{-1}	-8.55×10^{-2}

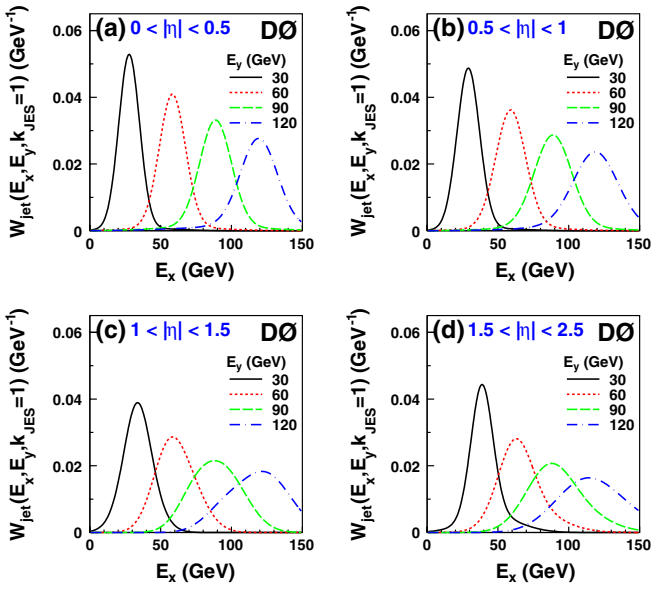

FIG. 2 (color online). Transfer functions for $k_{\mathrm{JES}} = 1$ light-quark jets as a function of measured jet energy for different parton energies in η regions: (a) $|\eta| < 0.5$, (b) $0.5 < |\eta| < 1.0$, (c) $1.0 < |\eta| < 1.5$, and (d) $1.5 < |\eta| < 2.5$.

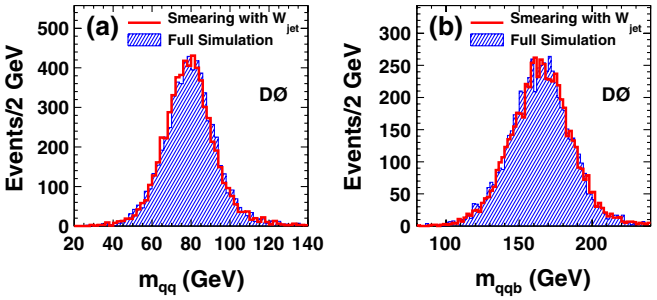

FIG. 3 (color online). Comparison of (a) 2-jet and (b) 3-jet invariant mass distributions for parton-level $t\bar{t}$ MC events with energies smeared using the transfer functions (open histogram) and fully simulated $t\bar{t}$ MC events with all four jets spatially matched to partons (filled histogram).

2. Parameterization of energy resolution for electrons

The electron energy resolution is parameterized by the transfer function

$$W_e(E_x, E_y) = \frac{1}{\sqrt{2\pi}\sigma} \exp\left[-\frac{1}{2}\left(\frac{E_x - E_y'}{\sigma}\right)^2\right], \quad (11)$$

where E_x is the reconstructed electron energy,

$$E_y' = 1.000 \cdot E_y + 0.324 \text{ GeV}, \quad (12)$$

$$\sigma = \sqrt{(0.028 \cdot E_y')^2 + (S \cdot E_y')^2 + (0.4 \text{ GeV})^2}, \quad (13)$$

TABLE III. Parameters for muon transfer functions for muon tracks with and without hits in the SMT.

Parameter	With hits in the SMT	No hits in the SMT
$\tilde{\sigma}_0$ (GeV^{-1})	2.082×10^{-3}	3.620×10^{-3}
$\tilde{\sigma}_1$	1.125×10^{-2}	1.388×10^{-2}
c_0 (GeV^{-1})	7.668×10^{-3}	2.070×10^{-2}
c_1	7.851×10^{-2}	7.042×10^{-2}

$$S = \frac{0.164 \text{ GeV}^{12}}{\sqrt{E_y'}} + \frac{0.122 \text{ GeV}^{12}}{E_y'} e^{C/\sin\theta_e} - C, \quad (14)$$

$$C = 1.3519 - \frac{2.0956 \text{ GeV}}{E_y'} - \frac{6.9858 \text{ GeV}}{E_y'^2}, \quad (15)$$

E_y is the energy of the original electron, and θ_e is the polar angle of the electron with respect to the proton beam direction. The parameters above are derived from the detailed modeling of electron energy response and resolution used in Ref. [34].

3. Parameterization of momentum resolution for muons

We describe the resolution of the central tracker through the uncertainty on the signed curvature of a track, the ratio of the electric charge and of the transverse momentum of a particle, parameterized as a function of pseudorapidity. The muon transfer function is parameterized as

$$W_\mu(\kappa_x, \kappa_y) = \frac{1}{\sqrt{2\pi}\sigma} \exp\left[-\frac{1}{2}\left(\frac{\kappa_x - \kappa_y}{\sigma}\right)^2\right], \quad (16)$$

where $\kappa_x = (q/p_T)_x$ and $\kappa_y = (q/p_T)_y$, with the charge q and transverse momentum p_T of the original muon (y) or its reconstructed track (x). The resolution

$$\sigma = \begin{cases} \tilde{\sigma} & \text{for } |\eta| \le 1.4 \\ \sqrt{\tilde{\sigma}^2 + \{c \cdot (|\eta| - 1.4)\}^2} & \text{for } |\eta| > 1.4 \end{cases} \quad (17)$$

is obtained from muon tracks in simulated events where the $\tilde{\sigma}$ and c parameters are linear functions of $1/p_T$:

$$\tilde{\sigma} = \tilde{\sigma}_0 + \tilde{\sigma}_1 \cdot 1/p_T, \quad (18)$$

$$c = c_0 + c_1 \cdot 1/p_T. \quad (19)$$

The values of the coefficients are given in Table III for muon tracks with associated and no associated hits in the silicon tracker. This simplified parameterization of the momentum resolution is valid at high transverse momenta ($p_T > 20$ GeV) where the limitations in coordinate resolution dominate over the effects of multiple scattering.

VI. CALIBRATION OF THE MEASUREMENT

The fully simulated MC samples described in Sec. IV are used in ensemble studies to calibrate the result from the

ME method by determining and correcting for biases in the extracted parameters and their estimated uncertainties. Such biases can be due, for example, to limitations in the LO ME used in Eq. (3) or to the imperfect description of detector resolution using transfer functions with a limited number of parameters. Five $t\bar{t}$ MC samples are generated for $m_t^{\rm gen} = 165$, 170, 172.5, 175, and 180 GeV, with two more produced from the 172.5 GeV sample by rescaling all jet energies by $\pm 5\%$. $P_{\rm sig}$ and $P_{\rm bkg}$ are calculated for these samples and for the W + jets MC samples. Events are drawn randomly from a $t\bar{t}$ sample with a particular mass and the W + jets sample to form pseudoexperiments, each with a number of events equal to the one observed in data (before requiring ≥ 1 b-tagged jets), with the signal fraction fluctuated according to a binomial distribution relative to that determined from data. The values of m_t and $k_{\rm JES}$ are extracted for each pseudoexperiment according to the procedure described in Sec. VA using only events with at least one b-tagged jet. A thousand pseudoexperiments are performed for each of the 7 $t\bar{t}$ samples. The means (and their uncertainties) of all 1000 measured values of m_t and $k_{\rm JES}$ in each sample are determined from Gaussian fits to their distributions and plotted versus the input $m_t^{\rm gen} - 172.5$ GeV and $k_{\rm JES} - 1$, respectively. A straight line is fitted to the plotted points, representing the response function used to correct the measurement from data (Fig. 4). For each pseudoexperiment, we also calculate the pulls, defined as $(m_t - \langle m_t \rangle)/\sigma(m_t)$ and $(k_{\rm JES} - \langle k_{\rm JES} \rangle)/\sigma(k_{\rm JES})$, where $\langle m_t \rangle$ and $\langle k_{\rm JES} \rangle$ are the mean measured m_t and $k_{\rm JES}$, respectively, for all pseudoexperiments, and $\sigma(m_t)$ and $\sigma(k_{\rm JES})$ are the rms of m_t and $k_{\rm JES}$, respectively, for the given pseudoexperiment. The width of the pull distributions for m_t and $k_{\rm JES}$ are shown as a function of $m_t^{\rm gen}$ and $k_{\rm JES}^{\rm gen}$ in Fig. 5. The average widths of the m_t and $k_{\rm JES}$ pull distributions are 1.08 and 1.07, respectively.

The signal fraction for the ensemble studies is determined from the selected data sample using the method described in Sec. VA. To correct for biases in the determination of this fraction, a calibration is done using the

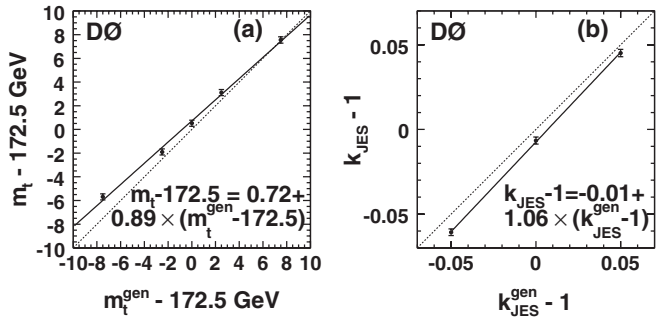

FIG. 4. Mean values of (a) m_t and (b) $k_{\rm JES}$ extracted from ensemble studies, as a function of the input values fitted to straight lines. Dashed lines represent 1:1 correlations of extracted and input values.

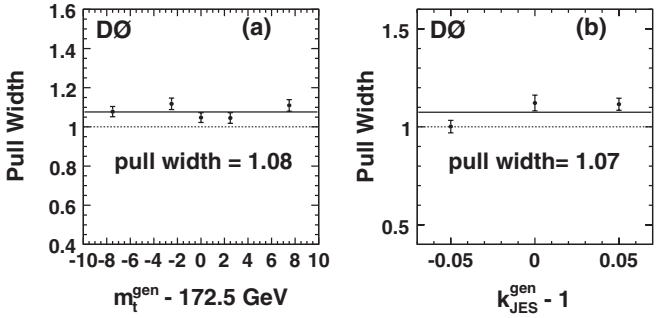

FIG. 5. Widths of the pull distributions for (a) m_t and (b) $k_{\rm JES}$ from ensemble studies as a function of the input values.

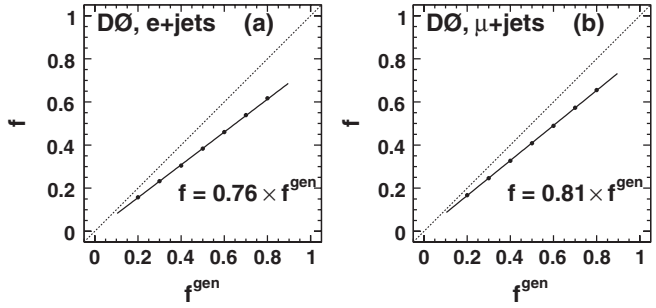

FIG. 6. Extracted signal fractions from ensemble studies as a function of the input values for the (a) e + jets and (b) μ + jets channels.

W + jets and 172.5 GeV $t\bar{t}$ MC samples, wherein 1000 pseudoexperiments are performed using the same procedure as described in the previous paragraph but with signal fractions set to a different value in each test. The extracted signal fractions as a function of their input values are shown in Figs. 6(a) and 6(b) for the e + jets and μ + jets channels, respectively. Straight lines are fitted to the points in plots representing the response functions used to correct the fractions determined from the selected data sample. The calibration of the signal fraction is performed separately for the e + jets and μ + jets channels. The corrected fractions are 0.35 ± 0.05 and 0.41 ± 0.06 for the e + jets and μ + jets channels, respectively, prior to requiring at least one b-tagged jet. These fractions are 0.71 ± 0.05 and 0.75 ± 0.04 for the e + jets and μ + jets channels, respectively, after requiring at least one b-tagged jet.

VII. FLAVOR-DEPENDENT JET-RESPONSE CORRECTION FOR MC EVENTS

The validity of the calibration procedure described in the previous section is based on the assumption of a perfect MC simulation of the events and of the detector. Uncertainties in this assumption are discussed in the section on systematic uncertainties (Sec. IX). The *in situ* jet energy scale employed in this analysis can account for a global scale discrepancy between data and MC jet energy

scales (see Sec. IX B 1) by rescaling the energies of the two light jets from the $W \to q\bar{q}'$ decay of $t\bar{t}$ events to the world average mass of the W boson [9]. This same rescaling is also applied to the two b jets in the event. However, jets originating from different partons have different kinematic characteristics and particle compositions. In particular, b and light jets with different electromagnetic fractions can lead to different responses in a noncompensating calorimeter. Such features, if not properly simulated, can result in a systematic shift in the determination of the top-quark mass. In fact, the largest contribution to the total systematic uncertainty of our previous analysis in Ref. [8] is the b/light-quark response ratio which was an estimate of the effect of such a discrepancy.

To bring the simulation of the calorimeter response to jets into agreement with data, and thereby reduce the systematic uncertainty associated with a jet-response difference in data and MC, we determine a flavor-dependent correction factor as follows. We note a discrepancy in the predicted energy deposition in the calorimeter between data and MC when we apply the single-particle responses from data and MC to the individual particles within MC jets that are spatially matched to reconstructed jets [35]:

$$\mathcal{D} = \frac{\sum E_i \cdot R_i^{\mathrm{Data}}}{\sum E_i \cdot R_i^{\mathrm{MC}}}, \tag{20}$$

where the sums run over each particle i in the MC particle jet, E_i is the true energy of particle i, and R_i^{Data} and R_i^{MC} are the single-particle responses in data and MC, respectively. We define a correction factor for a jet of flavor β(= light quark, gluon or b quark) as the ratio of the discrepancy for jets of flavor β to the flavor-averaged discrepancy for jets in γ + jet events, $F_{\mathrm{corr}}^{\beta} = \mathcal{D}^{\beta}/\langle \mathcal{D}^{\gamma+\mathrm{jet}} \rangle$. Defining the correction this way preserves the standard MC jet energy scale that is, strictly speaking, only appropriate for the γ + jet events from which it is derived. At the same time, it brings the relative response difference between jets of flavor β and jets in γ + jet events in MC into agreement with that in data. The quantity $F_{\mathrm{corr}}^{\beta} - 1$ is shown in Fig. 7 as a function of jet p_T and η for light-quark, gluon, and b jets. The shaded band at $F_{\mathrm{corr}}^{\beta} - 1 = 0$ in each plot corresponds to the correction for jets in γ + jet events. We apply these correction factors to the light-quark jets and b jets in a $t\bar{t}$ MC sample generated with $m_t^{\mathrm{gen}} = 172.5$ GeV, extract m_t and k_{JES} using our analysis technique, and compare them with the values extracted

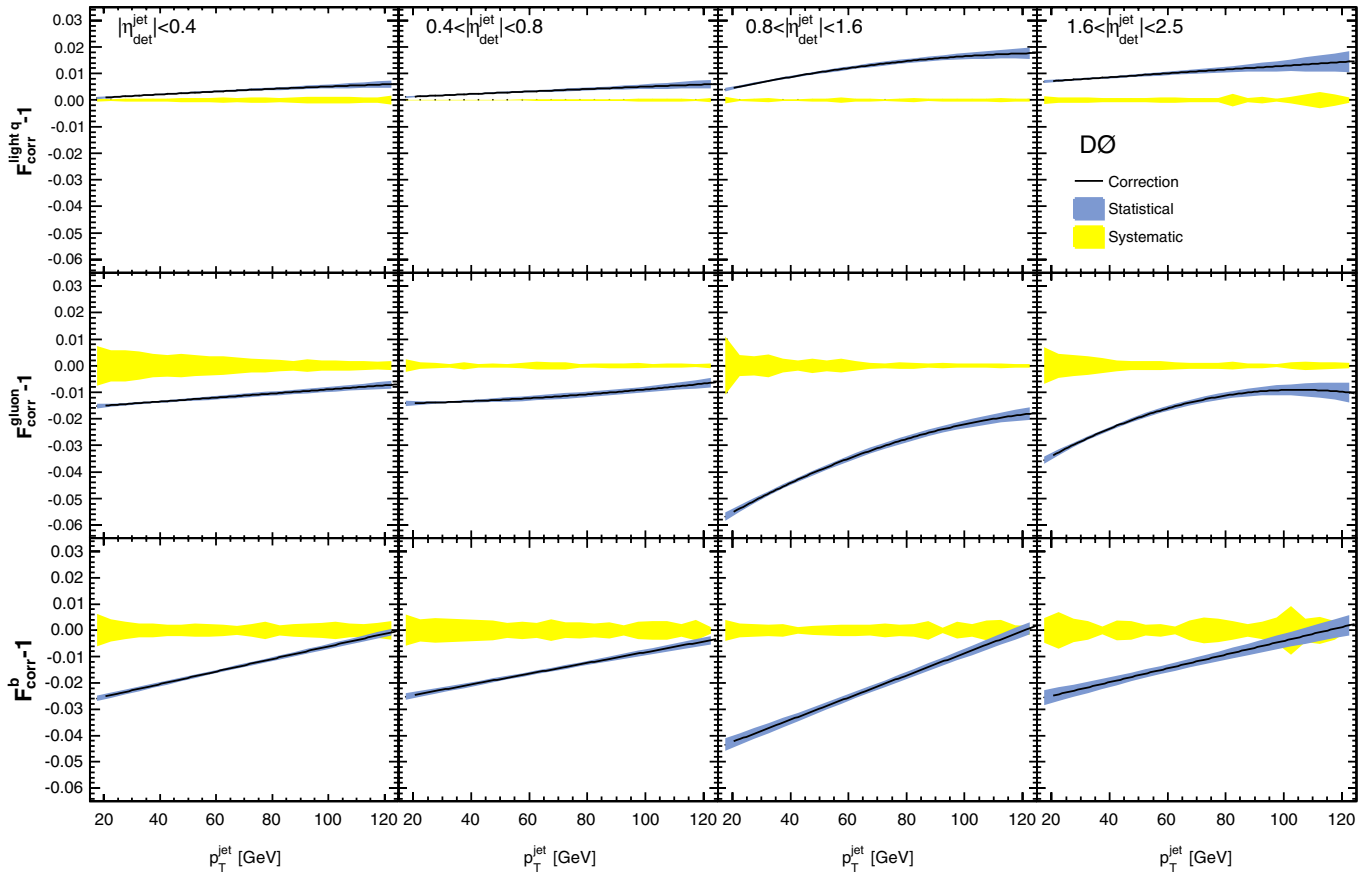

FIG. 7 (color online). Correction factors for data-MC jet-response difference for light-quark, gluon, and b jets as a function of jet p_T and η. Light shaded bands represent statistical uncertainties and dark shaded bands represent systematic uncertainties.

from the same set of events without using this correction. We find shifts of $\Delta m_t = -1.26$ GeV and $\Delta k_{\mathrm{JES}} = 0.005$ relative to the uncorrected sample. Repeating this study on a $t\bar{t}$ MC sample appropriate for the previous analysis [8] yields shifts of $\Delta m_t = -1.28$ GeV and $\Delta k_{\mathrm{JES}} = 0.005$.

VIII. MEASUREMENT OF THE TOP-QUARK MASS

The likelihoods $L(\tilde{x}; m_t)$ and $L(\tilde{x}; k_{\mathrm{JES}})$ for the selected data, calculated according to Eq. (6) and (7), respectively, are calibrated by replacing m_t and k_{JES} by parameters fitted to the response plots of Sec. VI:

$$m_t^{\mathrm{calib}} = \frac{(m_t - 172.5\ \mathrm{GeV}) - p_0^{m_t}}{p_1^{m_t}} + 172.5\ \mathrm{GeV}, \quad (21)$$

$$k_{\mathrm{JES}}^{\mathrm{calib}} = \frac{(k_{\mathrm{JES}} - 1) - p_0^{k_{\mathrm{JES}}}}{p_1^{k_{\mathrm{JES}}}} + 1, \quad (22)$$

where $p_i^{m_t}$ and $p_i^{k_{\mathrm{JES}}}$ are the parameters of the m_t and k_{JES} response functions shown in Fig. 4(a) and 4(b), respectively, and m_t and k_{JES} and their uncertainties are extracted from the mean and rms values of the calibrated likelihoods shown in Figs. 8(a) and 8(b). The extracted uncertainties for m_t and k_{JES} are multiplied by 1.08 and 1.07, respectively, to correct for deviations of the average pull widths from unity (see Sec. VI). Figure 9 shows the fitted Gaussian contours of equal probability for the two-dimensional likelihoods as a function of m_t and k_{JES}. We find $m_t = 174.75 \pm 1.28(\mathrm{stat} + \mathrm{JES})$ GeV and $k_{\mathrm{JES}} = 1.018 \pm 0.008(\mathrm{stat})$. Applying the shifts of $\Delta m_t = 1.26$ GeV and $\Delta k_{\mathrm{JES}} = -0.005$ described in Sec. VII yields a measured top-quark mass and jet energy scale factor of

$$\begin{aligned} m_t &= 176.01 \pm 1.28(\mathrm{stat} + \mathrm{JES})\ \mathrm{GeV} \\ &= 176.01 \pm 1.01(\mathrm{stat}) \pm 0.79(\mathrm{JES})\ \mathrm{GeV}, \\ k_{\mathrm{JES}} &= 1.013 \pm 0.008(\mathrm{stat}). \end{aligned}$$

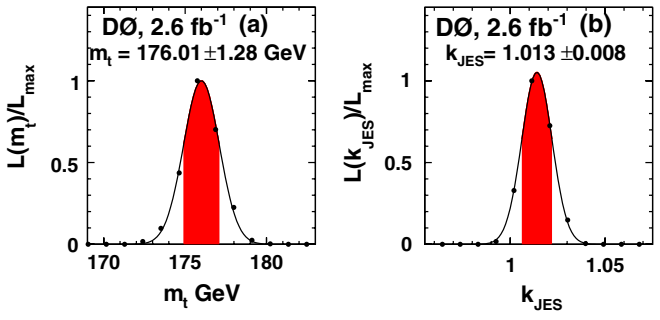

FIG. 8 (color online). Calibrated projections of the data likelihoods onto the (a) m_t and (b) k_{JES} axes with 68% confidence level regions indicated by the shaded areas. The values of m_t and k_{JES} shown in the figures are after applying all the corrections described in Sec. VII and VIII.

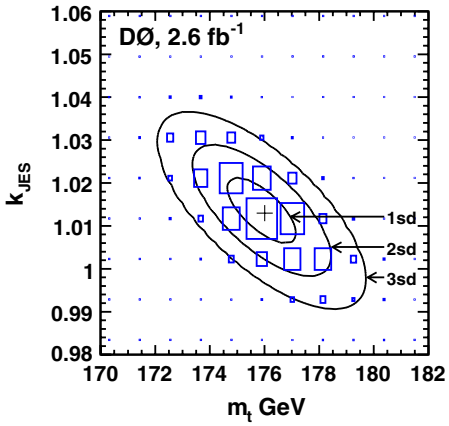

FIG. 9 (color online). Fitted contours of equal probability for the two-dimensional likelihood $L(\tilde{x}; m_t, k_{\mathrm{JES}})$.

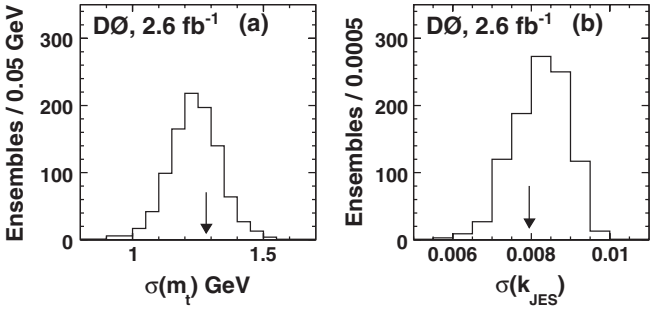

FIG. 10. Expected uncertainty distributions for (a) m_t and (b) k_{JES} determined from 1000 pseudoexperiments performed on the MC $t\bar{t}$ sample for $m_t^{\mathrm{gen}} = 175$ GeV. The measured uncertainties are indicated by the arrows.

Distributions in expected uncertainties, determined from 1000 pseudoexperiments performed on the MC $t\bar{t}$ sample for $m_t^{\mathrm{gen}} = 175$ GeV, are shown in Figs. 10(a) and 10(b) for m_t and k_{JES}, respectively. The measured uncertainties, indicated by the arrows, are within the expected range observed in MC and do not depend in any appreciable way on the assumed value of m_t.

IX. SYSTEMATIC UNCERTAINTIES

We evaluate systematic uncertainties for three categories. The first category, *modeling of production*, addresses uncertainties in the MC modeling of $t\bar{t}$ and W + jets production. The second category, *modeling of detector*, deals with the uncertainties in jet energy and lepton momentum scales and the simulation of detector response and any associated efficiencies. The third category involves uncertainties in the calibration of both m_t and the signal fraction f, and a possible bias from the exclusion of multijet events in MC ensemble studies. The contributions to the systematic uncertainty are summarized in Table IV. In the first three sections below, we describe the evaluation of

TABLE IV. Summary of systematic uncertainties.

Source	Uncertainty (GeV)
Modeling of production:	
Modeling of signal:	
Higher-order effects	±0.25
ISR/FSR	±0.26
Hadronization and UE	±0.58
Color reconnection	±0.28
Multiple $p\bar{p}$ interactions	±0.07
Modeling of background	±0.16
W + jets heavy-flavor scale factor	±0.07
Modeling of b jets	±0.09
Choice of PDF	±0.24
Modeling of detector:	
Residual jet energy scale	±0.21
Data-MC jet-response difference	±0.28
b-tagging efficiency	±0.08
Trigger efficiency	±0.01
Lepton momentum scale	±0.17
Jet energy resolution	±0.32
Jet identification efficiency	±0.26
Method:	
Multijet contamination	±0.14
Signal fraction	±0.10
MC calibration	±0.20
Total	±1.02

each of these contributions in more detail. In the fourth section, we discuss how systematic uncertainties from the previous analysis of 1 fb^{-1} of integrated luminosity [8] are updated to facilitate the combination of the two results presented in Sec. XI. Except for the *Data-MC jet-response difference* described in Sec. IX B 2, all of the systematic uncertainties described below are calculated prior to the flavor-dependent jet-response corrections of Sec. VII.

We adopt the following convention for systematic uncertainties δm_t in m_t and classify them into two types. The first type, referred to as the *Type I* uncertainty, is the effect of the ±1 sd variation of a relevant quantity. The second type, referred to as the *Type II* uncertainty, is due to the difference between models. For Type I uncertainties, we refer to the central or default value of the measurement as m_t^0 and to the measurement corresponding to the 1 sd (− 1 sd) variation as m_t^+ (m_t^-). We compute Type I uncertainties according to $\delta m_t = |m_t^+ - m_t^-|/2$ if $m_t^- < m_t^0 < m_t^+$ or $m_t^+ < m_t^0 < m_t^-$ and according to $\delta m_t = \max(|m_t^+ - m_t^0|/2, |m_t^- - m_t^0|/2)$ if $m_t^+ - m_t^0$ and $m_t^- - m_t^0$ have the same sign. We compute Type II uncertainties by taking the maximal difference between the models as the + and − systematic variations.

Many of our systematic uncertainties are evaluated by comparing two MC $t\bar{t}$ samples generated with the same input mass $m_t^{\rm gen}$. For these studies, we use samples with a value of $m_t^{\rm gen}$ close to the world average of m_t such as 172.5 GeV or 170 GeV.

A. Modeling of production

1. Higher-Order effects

The MC $t\bar{t}$ samples used to calibrate our measurement are generated using ALPGEN for the hard-scattering process and PYTHIA for shower evolution and hadronization (Sec. IV). We compare the LO generator ALPGEN with the next-to-leading order MC generator MC@NLO [36], in order to evaluate possible contributions from higher-order effects such as additional radiation of hard jets or gg contributions. We compare ALPGEN and MC@NLO MC $t\bar{t}$ samples with identical values of $m_t^{\rm gen}$ that both use HERWIG [37] for shower evolution and hadronization. HERWIG is used in both cases for consistency because MC@NLO can only be used with HERWIG (ALPGEN can be used with PYTHIA or HERWIG) and we are not interested in comparing different models for shower evolution and hadronization in this study. Ensemble studies are performed on both samples and the difference in the mean extracted m_t from ensembles for the two samples is found to be $m_t^{\rm MC@NLO} - m_t^{\rm ALPGEN} = 0.10 \pm 0.25$ GeV. Here, as in all the other systematic sources described below, when a shift in the value of the estimated parameter is statistically dominated, we replace the shift with its statistical uncertainty for the estimate of uncertainty. We, therefore, assign an uncertainty of ±0.25 GeV as the contribution from this source.

2. Initial state radiation/final state radiation

The uncertainties from this source are in the modeling of additional jets due to initial and final-state radiation (ISR/FSR). To evaluate this contribution, we compare three PYTHIA samples having identical values of $m_t^{\rm gen}$, with input parameters taken from a CDF ISR/FSR study based on the Drell-Yan process [38]. The three sets of parameters correspond to a fit to data and ±1 sd excursions. Half of the difference between the two excursions corresponds to a change in m_t of 0.26 ± 0.19 GeV.

3. Hadronization and underlying event

In simulating parton evolution and hadronization, PYTHIA and HERWIG model the parton showering, hadronization, and underlying event (UE) differently. To estimate the impact of this difference, we compare two MC $t\bar{t}$ samples with identical values of $m_t^{\rm gen}$, using ALPGEN for the hard-scattering process, but one sample using PYTHIA and the other using HERWIG for parton showering and hadronizaton. Ensemble studies indicate a difference in the means of the extracted m_t to be $m_t^{\rm PYTHIA} - m_t^{\rm HERWIG} = 0.58 \pm 0.25$ GeV.

4. Color reconnection

The MC samples used in this analysis do not simulate color reconnection for the final-state particles [39]. To evaluate the possible effect of color reconnection on the determination of m_t, we compare two MC $t\bar{t}$ samples with

identical values of $m_t^{\rm gen}$, using PYTHIA 6.4 tunes APRO and ACRPRO, which are identical except for the inclusion of color reconnection in ACRPRO. Ensemble studies of $t\bar{t}$ events performed on both samples yield a difference in the means of the extracted m_t of $m_t^{\rm Apro} - m_t^{\rm ACRpro} = 0.26 \pm 0.28$ GeV. We take the uncertainty on this difference and assign ± 0.28 GeV as the contribution from this source.

5. Modeling of jet mass

Unlike the jet algorithm used in Run I of Tevatron, the iterative midpoint cone algorithm used for Run II defines jets of intrinsic mass [21]. The effect of inaccuracies in the simulation of jet masses on the top-quark mass measurement is found to be negligible and is presently ignored.

6. Multiple $p\bar{p}$ interactions

Effects from additional $p\bar{p}$ interactions are simulated by overlaying on MC events unbiased triggers from random $p\bar{p}$ crossings. These overlaid events are then reweighted according to the number of interaction vertices to assure that the simulation reflects the instantaneous luminosity profile of the data. To evaluate the contribution from the uncertainty associated with the reweighting procedure, we repeat the ensemble studies used to derive the m_t calibration but without the reweighting. The rederived calibration is applied to $L(\tilde{x}; m_t)$ for the selected data sample, m_t is extracted and compared with the value from the default calibration, and found to shift by -0.07 GeV. This extreme check of the size of this contribution to the uncertainty shows that our result is not affected significantly by variations in luminosity.

7. Modeling of background

This systematic uncertainty receives contributions from two sources, one based on the data-MC discrepancy in background-dominated distributions and a second from uncertainty in the renormalization scale used to generate the W + jets samples. For the first source, we identify distributions in which there is poor agreement between data and MC in the modeling of background. Specifically, in both channels, we examine lepton p_T and the η of the jet of lowest p_T in the 3-jet multiplicity bin. Ensemble studies are performed on a sample of MC $t\bar{t}$ events using background events reweighted to match the distributions in data. The mean of the extracted m_t for this sample is found to shift by -0.03 GeV relative to that of the same MC $t\bar{t}$ events using the default background events.

The W + jets MC samples used in this analysis (Sec. IV) are generated using identical renormalization and factorization scales of $\mu = M_W^2 + \sum p_T^2$ where the sum is over the jets in an event. To evaluate the effect of the uncertainty in this scale, we generate two more W + jets MC samples with modified renormalization and factorization scales of $\mu/2$ and 2μ. We perform ensemble studies on a $t\bar{t}$ MC sample using these modified W + jets samples and find that the means of the extracted m_t shift by 0.13 GeV ($\mu/2$) and 0.32 GeV (2μ) relative to the studies using the default W + jets sample. We take half of the larger excursion and assign ± 0.16 GeV as the contribution from this source.

The contributions from the above data-MC discrepancy for the background and from the uncertainty on the scales are combined in quadrature for a total of systematic uncertainty of ± 0.16 GeV.

8. W + jets Heavy-flavor scale factor

The default heavy-flavor content in LO ALPGEN MC W + jets (Sec. IV) is increased by a factor of 1.47 for the $Wc\bar{c}$ + jets and $Wb\bar{b}$ + jets contributions to achieve agreement with NLO calculations of cross sections that include NLL corrections based on the MCFM MC generator [26]. To evaluate the uncertainty from this source, we shift this factor up to 1.97 and down to 0.97 and, for each variation, repeat the ensemble studies described in Sec. VI for the calibration of m_t, apply this to $L(\tilde{x}; m_t)$ in data, and reextract m_t. The shifts in m_t relative to the default value are found to be -0.07 GeV and 0.02 GeV when the scale factors are shifted up and down, respectively. We assign ± 0.07 GeV as the contribution from this source to the uncertainty of m_t.

9. Modeling of b jets

Possible effects in modeling b-quark fragmentation are studied by reweighting the simulated $t\bar{t}$ events used in the calibration of the measurement to simulate other choices of b-quark fragmentation models for the b jets. All the default MC samples used in this analysis consist of events that are reweighted from the default PYTHIA b-quark fragmentation function (based on the Bowler model [40]) to a Bowler scheme with parameters tuned to data collected at the LEP e^+e^- collider [41]. To evaluate the systematic uncertainty, these events are reweighted again to account for differences between LEP and SLAC e^+e^- data [41]. The ensemble studies of m_t are repeated using these reweighted events, the new calibration applied to $L(\tilde{x}; m_t)$ for data, and m_t extracted. m_t is found to shift by 0.08 GeV relative to the default value.

Additional differences in the response of b jets can be expected in the presence of semileptonic decays of b or c-quarks. The incorrect simulation of semileptonic b and c-quark decay branching fractions can therefore lead to a systematic shift in the extracted value of m_t. We take an uncertainty of ± 0.05 GeV determined in Ref. [42] as the contribution from this source.

Combining the two above uncertainties in quadrature gives ± 0.09 GeV, which we assign as the systematic uncertainty for the modeling of b jets.

10. Choice of PDF

We evaluate this systematic uncertainty using a PYTHIA MC $t\bar{t}$ sample that is reweighted to match possible excursions in the PDF parameters represented by the 20 CTEQ6M uncertainty PDFs [27]. Ensemble studies are repeated for each of these variants for only $t\bar{t}$ events and the uncertainty evaluated using the following formula [27]:

$$\delta m_t^{\mathrm{PDF}} = \frac{1}{2}\left(\sum_{i=1}^{20}[\Delta M(S_i^+) - \Delta M(S_i^-)]^2\right)^{1/2}, \qquad (23)$$

where the sum runs over PDF excursions in the positive (S_i^+) and negative (S_i^-) directions. $\delta m_t^{\mathrm{PDF}}$ is found to be 0.24 GeV.

B. Modeling of detector

1. Residual JES uncertainty

The *in situ* jet energy calibration employed in this analysis addresses a possible global scale difference in JES between data and MC. Any other discrepancy, such as a dependence on p_T and η, can have a systematic effect on the determination of m_t. To estimate this, the fractional uncertainty associated with the standard jet energy correction, derived using the γ + jet and dijet samples, is parameterized as a function of p_T and η. This uncertainty includes statistical and systematic contributions from both data and MC added in quadrature. All jet energies in a $t\bar{t}$ MC sample are then scaled up by the parameterized uncertainty as a function of p_T and η. The parameters are then shifted in such a way that the average scale shift applied to all jets vanishes. Ensemble studies are performed on the default and scaled samples, and the extracted m_t found to shift by 0.21 GeV relative to the default sample.

2. Data-MC jet-response difference

The uncertainties in the flavor-dependent jet-response correction for MC events (described in Sec. VII), used to bring the simulation of calorimeter response into agreement with that observed in the data, are associated with uncertainties in single-particle responses in data and MC. To evaluate the effect of these uncertainties on the value of m_t, we change the correction factors by ± 1 sd and apply them to the light jets and b jets in a $t\bar{t}$ MC sample. The value of m_t is extracted and the mean is found to shift by ± 0.28 GeV relative to the sample corrected using the central values.

3. b-Tagging efficiency

Discrepancies in the b-tagging efficiency between data and MC can lead to a systematic shift in the extracted m_t. To evaluate the effect of possible discrepancies, the tag rate functions for b and c quarks and the mistag rate function for light quarks are changed by 5% [23] and 20%, respectively, corresponding to the uncertainties on these functions. Ensemble studies for all $t\bar{t}$ MC samples are then repeated and the m_t calibration rederived and applied to data to extract m_t. The result is compared with that from the default calibration and found to shift by -0.08 GeV.

4. Trigger efficiency

The MC events used in this analysis have associated weights to simulate the effect of trigger efficiencies. To evaluate the effect of the uncertainties in these weights on the top-quark mass, we repeat the ensemble studies on all $t\bar{t}$ MC samples with the weights set to unity, rederive the m_t calibration, and apply it to the data to extract m_t. The result is found to shift by -0.01 GeV.

5. Lepton momentum scale

A relative difference in the lepton momentum scale between data and MC can have a systematic effect on m_t. To evaluate this, we first determine the size of the discrepancy and correct the scale of one $t\bar{t}$ MC sample. Ensemble studies are repeated on the corrected sample and the mean of the extracted m_t is found to shift by 0.17 GeV relative to the default sample.

6. Jet energy resolution

Since the jet transfer functions used are derived from MC samples, improper simulation of jet energy resolution can result in a bias in the extracted m_t. To evaluate a possible bias, ensemble studies are performed using a $t\bar{t}$ MC sample with jet energy resolutions degraded by 1 sd. The mean of the extracted m_t in this sample is found to shift by 0.32 GeV [43].

7. Jet identification efficiency

The uncertainties associated with the scale factors used to achieve data-MC agreement in jet identification efficiencies are propagated to the measurement of m_t by decreasing the jet identification efficiencies in a $t\bar{t}$ MC sample according to these uncertainties. We can only simulate a decrease and not an increase, as reconstructed jets can be dropped but not created. Ensemble studies indicate that the mean of the extracted m_t shifts by 0.26 GeV relative to that of the default sample [43,44].

C. Method

1. Multijet contamination

The multijet background is not included in the ensemble studies used to derive the calibrations described in Sec. VI as we have assumed that $P_{\mathrm{bkg}} \gg P_{\mathrm{sig}}$ for such events (see Sec. V A), resulting in a negligible influence on the determination of m_t. To evaluate possible systematic effects due to this assumption, we select a multijet-enriched sample of events from data by inverting the lepton isolation criterion

in the event selections. We repeat the ensemble studies to derive the m_t calibration using the multijet-enriched sample in the sample composition. The rederived calibration is applied to data, and the extracted m_t is found to shift by 0.14 GeV relative to the default calibration [44].

2. Signal fraction

The signal fractions determined from data and used in the ensemble studies have associated statistical uncertainties. These signal fractions are varied by their uncertainties, independently for each decay channel, and the ensemble studies repeated for all MC samples to rederive the m_t calibration shown in Fig. 4(a). The new calibrations are then applied to the data and results compared with those obtained using the default calibration. The resulting uncertainties in m_t evaluated by changing the signal fractions in each decay channel are then added in quadrature and divided by two to obtain a total of ± 0.10 GeV.

3. MC calibration

We estimate the effect of the statistical uncertainties associated with the offset and slope parameters determined from the fit to the response plot shown in Fig. 4(a). To estimate this uncertainty, we change these two parameters, one at a time, by their uncertainties and apply the modified calibration to the data to extract m_t and calculate the difference relative to the m_t extracted using the default calibration. We combine, in quadrature, the differences in m_t resulting from such changes in each parameter and find an uncertainty of ± 0.20 GeV.

D. Treatment of systematic uncertainties in previous analysis

To facilitate the combination of the new measurement with the previous one, we have updated the systematic uncertainties presented in Table I of Ref. [8]. All of the uncertainties in this table are unchanged, except for the uncertainties in the modeling of signal and the relative b/light-quark response ratio. The uncertainty for the modeling of signal in the previous analysis is replaced with one from the current analysis, which includes contributions from uncertainties in the modeling of higher-order effects, ISR/FSR, hadronization and underlying event, color reconnection, and multiple hadron interactions. The uncertainty on b/light-quark response is replaced with that associated with differences in jet response in data and MC for the current analysis (see also Sec. VII). The uncertainty in the modeling of background in Table I of Ref. [8] is the sum in quadrature of (i) the uncertainty in the heavy-flavor scale factor, and (ii) the uncertainty associated with discrepancies between data and MC background distributions. Since the uncertainty on the renormalization and factorization scale was not evaluated in the previous analysis, we include the additional contribution described in the second part of Sec. IX A 7. We also evaluate the uncertainty associated with the flavor-dependent jet-response correction factors appropriate for the previous analysis, using the procedure described in Sec. IX B 2. We find the mean of the extracted m_t shifts by 0.13 GeV (-0.22 GeV) relative to the sample corrected with the central values when we change the correction factors by 1 sd (-1 sd). We assign ± 0.22 GeV as the contribution from this source. Adding the contributions from all sources in quadrature gives a total of ± 0.97 GeV.

X. RESULT OF THE CURRENT MEASUREMENT

We measure the mass of the top quark in $t\bar{t}$ lepton + jets events using a matrix-element method that combines an *in situ* jet energy calibration with additional information from the standard jet energy scale derived from γ + jet and dijets samples. Using data corresponding to 2.6 fb^{-1} of integrated luminosity collected by the D0 experiment from Run II of the Tevatron collider, we extract the value

$$m_t = 176.01 \pm 1.01(\text{stat}) \pm 0.79(\text{JES}) \pm 1.02(\text{syst}) \text{ GeV}$$

or $m_t = 176.01 \pm 1.64$ GeV.

XI. COMBINATION WITH THE PREVIOUS MEASUREMENT

Our result from a previous measurement using the same analysis technique, and based on earlier data corresponding to 1 fb^{-1} of integrated luminosity, is $m_t = 171.5 \pm 1.76(\text{stat + JES}) \pm 1.1(\text{syst})$ GeV [8]. Applying the shift of $\Delta m_t = 1.28$ GeV described in Sec. VII, and using updated systematic uncertainties described in Sec. IX D, yields

$$m_t = 172.74 \pm 1.44(\text{stat}) \pm 1.05(\text{JES}) \pm 0.97(\text{syst}) \text{ GeV}$$

or $m_t = 172.74 \pm 2.03$ GeV.

We combine the two measurements using the Best Linear Unbiased Estimator (BLUE) method [45,46] to get a result equivalent to 3.6 fb^{-1} of integrated luminosity. The combined value of the mass is

$$m_t = 174.94 \pm 0.83(\text{stat}) \pm 0.78(\text{JES}) \pm 0.96(\text{syst}) \text{ GeV}$$

or $m_t = 174.94 \pm 1.49$ GeV. The procedure we follow uses the same method and classes of uncertainty as used by the Tevatron Electroweak Working Group [5] in combining individual measurements for Tevatron averages of the top-quark mass.

ACKNOWLEDGMENTS

We thank the staffs at Fermilab and collaborating institutions, and acknowledge support from the DOE and NSF (USA); CEA and CNRS/IN2P3 (France); FASI, Rosatom and RFBR (Russia); CNPq, FAPERJ, FAPESP and

FUNDUNESP (Brazil); DAE and DST (India); Colciencias (Colombia); CONACyT (Mexico); KRF and KOSEF (Korea); CONICET and UBACyT (Argentina); FOM (The Netherlands); STFC and the Royal Society (United Kingdom); MSMT and GACR (Czech Republic); CRC Program and NSERC (Canada); BMBF and DFG (Germany); SFI (Ireland); The Swedish Research Council (Sweden); and CAS and CNSF (China).

[1] S. Abachi *et al.*(D0 Collaboration), Phys. Rev. Lett. **74**, 2632 (1995).
[2] F. Abe *et al.* (CDF Collaboration), Phys. Rev. Lett. **74**, 2626 (1995).
[3] The ALEPH, CDF, D0, DELPHI, L3, OPAL, SLC Collaborations, the LEP Electroweak Working Group, the Tevatron Electroweak Working Group, the SLD electroweak, and heavy flavour groups, arXiv:1012.2367; LEP Electroweak Working Group, http://lepewwg.web.cern.ch/LEPEWWG/.
[4] S. Heinemeyer *et al.*, J. High Energy Phys. 09 (2003) 075.
[5] The Tevatron Electroweak Working Group, arXiv:1007.3178; Tevatron Electroweak Working Group, http://tevewwg.fnal.gov.
[6] Events with $W \to \tau\nu$ decays can pass our selection criteria when the τ lepton decays leptonically. This is accounted for by including the simulation of $W \to \tau\nu$ decays in the MC samples used to calibrate the measurement.
[7] In the SM, the top-quark decays via $t \to Wb$ 100% of the time.
[8] V. M. Abazov *et al.* (D0 Collaboration), Phys. Rev. Lett. **101**, 182001 (2008).
[9] K. Nakamura *et al.* (Particle Data Group), J. Phys. G **37**, 075021 (2010).
[10] M. L. Mangano *et al.*, J. High Energy Phys. 07 (2003) 001.
[11] T. Sjöstrand *et al.*, Comput. Phys. Commun. **135**, 238 (2001); T. Sjöstrand, S. Mrenna, and P. Skands, J. High Energy Phys. 05 (2006) 026.
[12] A. Buckley *et al.*, arXiv:1101.2599.
[13] V. M. Abazov *et al.*, arXiv:1104.2887.
[14] V. M. Abazov *et al.* (D0 Collaboration), Nucl. Instrum. Methods Phys. Res., Sect. A **565**, 463 (2006).
[15] S. N. Ahmed *et al.*, Nucl. Instrum. Methods Phys. Res., Sect. A **634**, 8 (2011).
[16] The previous measurement in Ref. [8] is based on data corresponding to 1 fb^{-1} of integrated luminosity recorded before the installation of Layer 0 while the new measurement presented here is based on data corresponding to 2.6 fb^{-1} of integrated luminosity recorded after this installation.
[17] R. Angstadt *et al.*, Nucl. Instrum. Methods Phys. Res., Sect. A **622**, 298 (2010).
[18] V. M. Abazov *et al.*, Nucl. Instrum. Methods Phys. Res., Sect. A **552**, 372 (2005).
[19] M. Abolins *et al.*, Nucl. Instrum. Methods Phys. Res., Sect. A **584**, 75 (2008).
[20] The separation in $\eta - \phi$ space between objects a and b is defined as $\Delta\mathcal{R} = \sqrt{(\eta_a - \eta_b)^2 + (\phi_a - \phi_b)^2}$.
[21] G. C. Blazey *et al.*, arXiv:hep-ex/0005012.
[22] Particle jets are defined as the objects, consisting of stable final-state particles originating from the hard-scattering process or the underlying event, found by applying the jet reconstruction algorithm on these particles instead of the calorimeter cell towers.
[23] V. M. Abazov *et al.* (D0 Collaboration), Nucl. Instrum. Methods Phys. Res., Sect. A **620**, 490 (2010).
[24] These values are valid for the specific settings of the NN b-tagging algorithm chosen in this analysis.
[25] M. L. Mangano *et al.*, J. High Energy Phys. 01 (2007) 013.
[26] J. M. Campbell and R. K. Ellis, Nucl. Phys. B, Proc. Suppl. **205**, 10 (2010).
[27] J. Pumplin *et al.*, J. High Energy Phys. 07 (2002) 012.
[28] CERN Application Software Group, W5013, 1993.
[29] V. M. Abazov *et al.* (D0 Collaboration), Nature (London) **429**, 638 (2004).
[30] The 24 independent variables are associated with the vector momenta of the two initial-state and six final-state particles, whose masses are assumed known. Ten constraints are imposed if the direction vectors of the lepton and four final-state quarks are known precisely. This leaves 14 variables involving the vector momenta of the two inital state particles and the ν and the magnitude of the momenta of the four quarks and the ℓ. Conservation of energy and momentum imposes four additional constraints, eliminating the longitudinal components of the two intial state particles and the transverse components of the ν, leaving ten variables. For reasons indicated subsequently in the text, we replace these ten variables with the magnitudes of the momenta of the ℓ and of one of the light q from the W boson, the four transverse components of the two initial-state partons, the masses of the two W bosons and of the top quarks.
[31] F. A. Berends *et al.*, Nucl. Phys. B **357**, 32 (1991).
[32] S. Koonin and D. Meredith, *Computational Physics* (Addison-Wesley Publishing Company, Reading, MA, 1990).
[33] Soft muon tagging refers to the identification of b-jet candidates by searching within jets for the presence of relatively low momentum muons originating from semimuonic b decays.
[34] V. M. Abazov *et al.* (D0 Collaboration), Phys. Rev. Lett. **103**, 141801 (2009).
[35] We apply separate single-particle responses for the following particles: γ, $e^{\pm}$, $\mu^{\pm}$, $\pi^{\pm}$, $K^{\pm}$, K^0_S, K^0_L, $p/\bar{p}$, $n/\bar{n}$, and $\Lambda^0/\bar{\Lambda}^0$.
[36] S. Frixione and B. R. Webber, J. High Energy Phys. 06 (2002) 029.
[37] G. Corcella *et al.*, J. High Energy Phys. 01 (2001) 010.

[38] CDF collaboration (private communication) with; A. Abulencia *et al.* (CDF Collaboration), Phys. Rev. D **73**, 032003 (2006).
[39] D. Wicke and P. Z. Skands, Nuovo Cimento Soc. Ital. Fis. B **123**, 1 (2008).
[40] M. G. Bowler, Z. Phys. C **11**, 169 (1981).
[41] Y. Peters, K. Hamacher, and D. Wicke, Report No. Fermilab-TM-2425-E, 2006.
[42] V. M. Abazov *et al.* (D0 Collaboration), Phys. Rev. D **74**, 092005 (2006).
[43] Although this is a Type I uncertainty described in the introduction of Sec. IX, we do not take half of this value as the change is only evaluated in one direction.
[44] These systematic uncertainties are taken from Ref. [8].
[45] L. Lyons, D. Gilbaut, and P. Clifford, Nucl. Instrum. Methods Phys. Res., Sect. A **270**, 110 (1988)
[46] A. Valassi, Nucl. Instrum. Methods Phys. Res., Sect. A **500**, 391 (2003).